ABSTRACT

Title of Document: MINIATURE LOW-COHERENCE FIBER OPTIC ACOUSTIC SENSOR WITH THIN-FILM UV POLYMER DIAPHRAGM

Felix Stief, Master of Science, 2012

Directed By: Associate Professor Miao Yu
Sensors and Actuators Laboratory
Department of Mechanical Engineering

A miniature low-coherence fiber optic acoustic sensor with a thin-film UV polymer diaphragm is developed and studied in this thesis to address the fundamental challenge of miniaturizing acoustic sensors. When miniaturizing an acoustic sensor, there is a critical size limitation at which the transduction mechanism deformation becomes too small for detection. However, a solution to this problem is to utilize a high resolution, low coherence fiber optic interferometric detection system coupled with a soft, thin-film transduction mechanism. A novel fabrication technique was developed to enable the use of elastomers, which inherently exhibit desirably low Young's modulus properties. In addition, the fabrication process enables fabrication of diaphragms at thicknesses on the order of nanometers. The fabrication process also renders highly tunable sensor performance and superior sensing quality at a low cost. The sensor developed exhibits a flat frequency response between 50 Hz and 4

kHz with a useable bandwidth up to 20 kHz, a dynamic range of 117.55 dB SPL, a signal to noise ratio (SNR) of 58 dB, and a sensitivity up to 1200 mV/Pa. In this thesis, it is further demonstrated that by using an array these sensors fabricated from the same batch facilitates accurate directional sound localization by utilizing the interaural phase difference (IPD) exhibited by sensor pairs. Future work is suggested to optimize the sensor performance for a specific application, to carry out studies of more complex array configurations, and to develop algorithms that can help increase the sound localization accuracy.

MINIATURE LOW-COHERENCE FIBER OPTIC ACOUSTIC SENSOR WITH THIN-FILM UV POLYMER DIAPHRAGM

By

Felix Stief

Thesis submitted to the Faculty of the Graduate School of the
University of Maryland, College Park, in partial fulfillment
of the requirements for the degree of
Master of Science
2012

Advisory Committee:
Assistant Professor Miao Yu, Chair and Adviser
Professor Don DeVoe
Assistant Professor Sarah Bergbreiter

DEDICATION

To my parents

ACKNOWLEDGMENTS

I am very grateful to my advisor, Professor Miao Yu, for her continuous encouragement, guidance, patience, and staunch confidence in my abilities throughout the entirety of my graduate experience. I am thankful that she continuously challenged me and I am certain that everything I learned under her guidance will help me succeed in my future career and endeavors. I am also thankful to Professor Yu for the opportunity to present in front of consortium and proof of concept alliances, which were wonderful learning experiences.

I would also like to extend my gratitude to my committee members, Professor Don DeVoe and Professor Sarah Bergbreiter for their willingness to serve on my committee and for reviewing my dissertation.

I am very fortunate to be in the same lab group with Dr. Yuxiang Liu, Haijun Liu, Hyungdae Bae, Cheng Pang, Laith Sawaqed, Andrew Lisiewski, and Sungmin Park. Their friendship, encouragement, suggestions, and discussions have been instrumental to my personal growth and success.

I am thankful for the support received from the Army Research Laboratory Acoustics Group, who volunteered their time and facilities to aid in the performance characterization of the sensor developed in this thesis.

TABLE OF CONTENTS

LIST OF FIGURES

LIST OF TABLES

1 Introduction and Background

1.1 Problem of Interest

Acoustic sensing is a desirable attribute utilized in many civilian applications ranging from structural health monitoring of bearings [1] and buildings [2] to noise pollution monitoring and mapping [3], as well as multiple applications on the modern battlefield [4]. Battlefield applications include autonomous robot navigation, search and rescue vehicles and peripherals, targeting systems, and gunshot localization.

All of the previously mentioned applications would benefit from miniaturized sensors by making the sensors more portable, lighter, and less expensive. For sound source localization purposes, array based sound arrangements offer increased versatility and the ability to operate in the near field. For near field operations, the microphone separation distance should be small enough to compensate the effects of the sound wave-front curvature, which can only be achieved with small sensors. For these reasons, developing miniature acoustic sensors and sensor arrays become an important task.

While desirable, acoustic sensor miniaturization is a difficult objective to achieve. The low sound pressure must be detected using a transduction mechanism, which in most acoustic sensor designs, employs a thin diaphragm. The diaphragm diameter determines the size of the microphone, while the diaphragm deflection is related to the microphone's sensitivity. The challenge is to design a microscale diaphragm that is sensitive enough to low dynamic pressures, while offering a large bandwidth. To construct a large array with many small microphones, the sensors should be inexpensive while maintaining high sensor-to-sensor uniformity. This poses a challenge to the sensor fabrication.

Compared to traditional electronic sensing techniques, optical sensing techniques offer immunity to electromagnetic interference, better performance in hazardous and explosive environments, and most importantly, inherently good performance characteristics, such as high accuracy, high bandwidth, and fast response time. An acoustic sensor utilizing optical sensing techniques is therefore of great interest for miniaturization.

1.2 Previous Work

The term ‘microphone’ applies to acoustic sensors that operate in the audible range, which generally ranges from several Hz to 20 kHz. Over this broad spectral range, a microphone measures acoustic pressure by detecting the vibration motion of a diaphragm [5]. Microphones differ by performance characteristics, such as sensitivity, bandwidth, and dynamic range, partially due to differences in detection mechanisms, such as piezoelectric, piezoresistive, capacitive, and optical [6]. Since the scope of this thesis is limited to optical acoustic sensors, other transduction mechanisms will henceforth not be elaborated upon.

1.2.1 Fiber-optic microphones

Research and development of optical microphones has been carried out for almost 30 years. Initial research interest was sparked by a laser Doppler microphone by Hess in 1992 [7]. Since then, the two most commonly published acoustic sensor designs are based on detecting the deflection of a diaphragm utilizing a Fabry-Pérot interferometer [8–17] or intensity based interrogation techniques [18–24]. Fiber Bragg Gratings (FGSs) [25,26] and various single fiber sensing methods [27–42] have also been

employed in fiber optic acoustic sensors. The choice of signal-processing technique significantly affects the resolution, sensitivity to noise ratio, dynamic response, and other microphone performance properties [43].

Fabry-Pérot Interferometer Based Microphones

A Fabry-Pérot Interferometer (FPI) is the most commonly used configuration for optical microphones. FPIs consist of two parallel partial mirrors separated by a short distance. This distance can be modulated by external forces resulting in a phase shift between the beams reflected from the two mirrors. The interference of these reflected beams can be analyzed to determine the change in distance between the two partial mirrors. Considering a FPI where the distance between *Mirror 1* and *Mirror 2* (i.e., the cavity length), as shown in Figure 1-1, is denoted as *L*, and the phase of the light, □, passing through the Fabry-Pérot cavity is given by

$$\Phi = \beta L, \tag{1.1}$$

where

$$\beta = n_{eff} k_0. \tag{1.2}$$

Here, n_{eff} represents the average refractive index of the fiber's core, and k_0 is the wavenumber, defined as $2\pi/\lambda$. Since β is as fixed parameter unless the wavelength, λ, of

the light source is modulated, or the refractive index of the cavity is changed, the simplest option to modulate the phase is to change the distance between the mirrors, *L*. Regardless of application, FPI sensors are known for their high sensitivity, immunity to electromagnetic interference, small size, low cost, versatility, reliability, and potential for multiplexing [44].

FPIs can be further subcategorized into Internal Fabry-Pérot Interferometers (IFPI) and External Fabry-Pérot Interferometers (EFPI). In an IFPI configuration, shown in Figure 1-2, light never exits the waveguide and a change in Optical Path Difference (OPD) is achieved by modulating the waveguide itself. IFPI-based microphones are not very common since modulating the length of a fiber is not easy due to the large Young's modulus of silica; this in turn requires long, bulky spools of fiber to ensure enough sensitivity for picking up acoustic perturbations.

An example of IFPI based microphone configuration is presented by Yoshino *et*

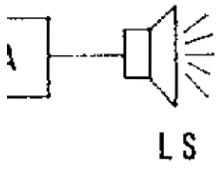

al [9]. The schematic of the system is shown in Figure 1-3. The laser is coupled into a 100 m long Fiber Fabry-Pérot Interferometer (FFPI), coiled in a 30 cm diameter, and fixed to a metal plate, which acts as a resonator to enhance the acoustic vibrations of the fiber. The vibrations modulate the length, *L*, of the optical cavity, which is formed by two polished and coated end faces of the 100 m single mode fiber [9]. A complex electrical system is employed to retain the optimal operating conditions (quadrature point) of the system by compensating for thermal drift. The bandwidth of the system has only been demonstrated experimentally to cover between 1 and 10 kHz, and therefore does not reach the upper and lower bounds of human hearing (20 Hz – 20 kHz). While the system is capable of multiplexing, the size of the sensor element, the need for a resonating mount, the expensive long coherence length laser diode (LD), and the complex control system make it impractical for commercial applications.

Due in large to the smaller size and good performance characteristics of EFPIs, many efforts have been focused on developing EFPI based microphones. EFPIs are composed of two partial mirrors separated by an air gap. The advantage of this configuration is that the material and size of the second partial mirror is not restricted to

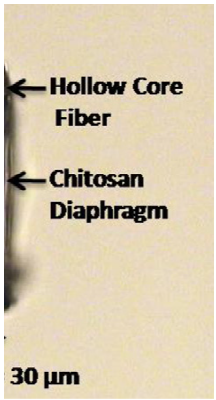

coustic sensor [8]

that of a waveguide. As a result, there is a plethora of configurations, the most recent ranging from fiber-diameter size [8] to a slightly larger ferrule-diameter size [10–16] and utilizing diaphragm materials from Mylar-based film [12] to micro-machined silicon [11,17], to silica [10] [13] [14]. This makes the EFPI configuration much more tunable to specific applications. For these reasons, among others, this is the sensor configuration chosen for the development of the sensor presented in this thesis.

The most promising and comparable work to the contents of this thesis is presented by Chen *et al.* [8]. As shown in Figure 1-4, the sensor has a small size; the outer diameter is equivalent to that of the optical fiber. Other groups have developed sensors on the same size scale; however, they lack the ability to measure dynamic acoustic pressure over a reasonably wide bandwidth. While the small scale of the sensor is desirable, it also increases the complexity of the fabrication process. The cavity length is determined by a 30 micrometer long piece of 125 micrometer diameter multimode fiber that has been selectively etched to remove the core as shown in Figure 1-4 (b). At these scales, cleaving two parallel endfaces becomes difficult and time-consuming with a low success rate. Furthermore, the cavity length may not be adjusted to increase the performance of the sensor after fabrication. The diaphragm itself requires a custom chamber and multiple potentially dangerous ingredients, such as Potassium Chloride (KCl) and Dimethylformamide (DMF), to be synthesized over a duration of multiple hours per batch. The fabrication process, while tedious, yields a permeable diaphragm with a relatively low Young's modulus of 2-4 GPa [8]. Thus, while the approach detailed by Chen *et al.* retains a small form factor with reasonable performance, the sensor cannot be batch fabricated.

The work by Chen *et al.* appears to be an extension of the pressure sensor developed by Cibula *et al.* The sensor developed by Cibula *et al.* exhibits the same design elements as shown in Figure 1-5; the cavity housing is spliced and etched from a multimode fiber, and the diaphragm fabrication requires a specialized drying chamber and the use of dangerous chemicals. The diaphragm fabricated by Cibula *et al.* did not exhibit detectable deflections at typical acoustic pressure fluctuations due to the large Young's modulus of the diaphragm.

Intensity Based Microphones

Several groups have developed intensity modulated acoustic pressure sensors, the most common design consisting of a hexagonal array of six collecting fibers and one central light emitting fiber all facing a reflective diaphragm. The light intensity reflected by the diaphragm is coupled into the collecting fibers, which is proportional to the deflection of the diaphragm. A schematic of such a device is shown in Figure 1-6. Typically, increasing the number of fibers in the bundle results in improved performance; using more fibers however also increase the size and cost of the device. Previous studies

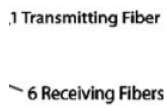

suggest that fibers with large core radii, large numerical aperture, and small fiber cladding are preferred [18]. Compared to interference-based sensors, this design yields lower sensitivity and resolution in addition to being relatively large in size. The advantages are ease of fabrication and low cost [18,21–24,45–47].

The most notable recent work for intensity based microphones is reported by Bucaro *et al.* This microphone was similar to another device developed earlier by Bucaro and Lagakos [23]. It was also inspired by multifiber probe lever microphones introduced by He and Cuomo [18], Hu *et al.* [46], and Zuckerwar *et al.* [22]. The microphone utilizes a 1.5 μm thick, microfabricated low stress single-crystal Silicon (Si) diaphragm with a diameter of 1.6 mm. Another Silicon structure of 2.8 mm diameter is used to support the diaphragm and fix the diaphragm to a metal tube containing a hexagonal array of seven fibers. A special technique is developed to allow for precise fiber-to-diaphragm gap distance adjustment, thereby controlling the final sensitivity of the sensor. Performance is desirably uniform over the range from 1 kHz to 20 kHz with the first natural frequency close to 24 kHz. The sensor developed thus performs very well, which is to be expected given its relatively large size. The sensor design permits easy performance parameter customization, yet the fabrication requires expensive equipment.

Fiber Bragg Grating Based Microphones

Fiber Bragg Gratings (FBGs) are composed of intrinsic distributed Bragg reflectors. Bragg reflectors are created by periodically varying the refractive index of the fiber core. The periodicity, or pitch of the reflectors, generates wavelength specific dielectric mirror. Modulating the reflector spacing by applying a tensile strain to the fiber results in a shift of reflected wavelength. The reflected wavelength, or Bragg wavelength, λ_B, not only depends on the grating period, Λ, but also its effective refractive index, n, as described by

$$\lambda_B = 2n\Lambda \quad (1.3)$$

The effective refractive index is governed by the strain-optics effect, while the grating period on the other hand is most responsive to physical strain or thermal effects. Due to the large Young's modulus, E, of the optical fiber, acoustic pressure fluctuations cannot simply be detected by using a FBG. To realize an optical acoustic sensor, the FBG must be coupled with a mechanical transduction element, like a diaphragm or a beam.

Two groups have reported optical microphones utilizing FBG sensing mechanisms. The earlier work by Iida *et al.* utilizes the deflection curvature of a 1 inch Titanium condenser microphone diaphragm with a thickness of 15 microns. The FBG is flush-mounted with the diaphragm as shown in Figure 1-7 (a) such that a diaphragm deflection bends the FBG, modulating the grating period. This in turn results in a Bragg wavelength shift. The performance of the microphone is poor compared to electrical counterparts; the frequency response curve of the microphone exhibits natural frequencies around 400 Hz and 5 kHz with no data provided above 10 kHz. An advantage of this design however is the ability to multiplex. The experimental results of

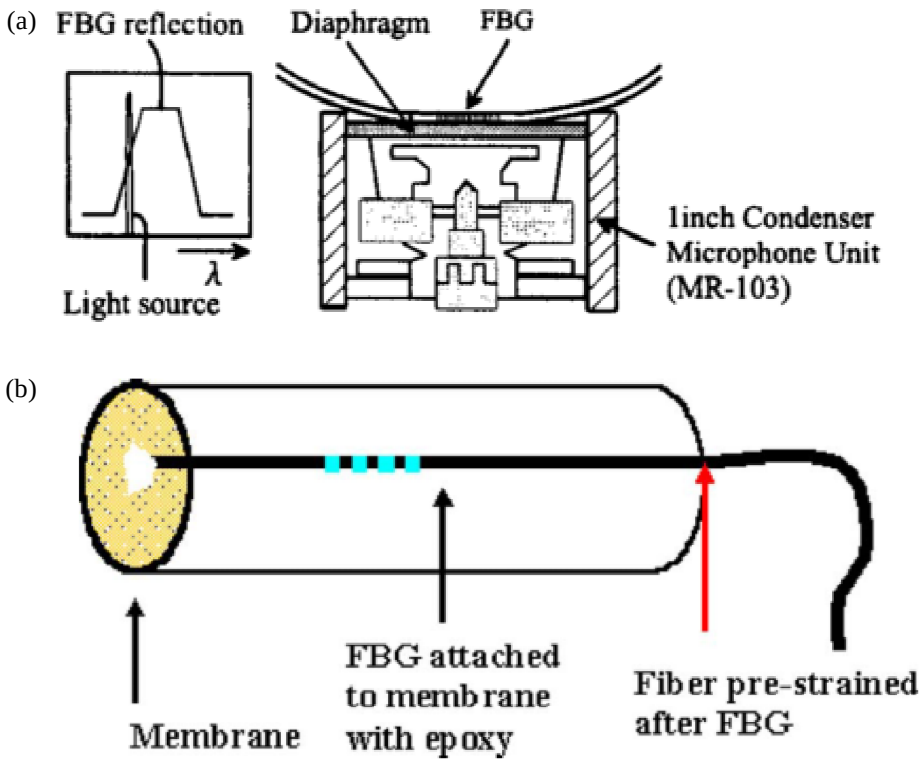

Figure 1-7. FBG-based microphone configuration by (a) Iida *et al.* [25] and Mohanty *et al.* [26].

four multiplexed microphones were obtained by utilizing a special wavelength division multiplexing (WDM) detection system. While preferred for distributed sensing, the system itself is complex, expensive, and limited in bandwidth [25].

The work by Mohanty *et al.* utilizes an alternate microphone configuration where a FBG is longitudinally attached to the diaphragm. The working principle is equivalent to that of the above mentioned work; the acoustic vibrations of the diaphragm induce a strain in the FBG which in turn results in a Bragg grating shift. The magnitude of the grating shift is proportional to the acoustic pressure. The design takes advantage of a 16 mm polymer diaphragm stretched over a cylindrical tube as shown in Figure 1-7 (b). A prestrained FBG is epoxied to the diaphragm and the other end of the tube. The optical system consists of a broadband light source that supplies light to the sensor. The reflected light is split into two beams, one of which is filtered with a linear edge filter,

serving as the reference beam. The other beam fluctuates according to the strain induced Bragg wavelength. Photodetectors transduce the optical signal to the electric domain and a differential amplifier is used to compare the signals. The output can be detected by an oscilloscope. The performance of the sensor is still rather poor, considering the large size of the sensor. The first resonant frequency is approximately 1 kHz and no measurements beyond 10 kHz were demonstrated. [26]

Acoustic Sensors Based on Single Fiber Sensing Methods

Single fiber sensing methods dominated the research focus during the infancy stage of fiber optic research. Currently, very few groups spent their efforts on developing these technologies. Due to this dearth in recent research progress, each technique will only be mentioned briefly. Schematics of each sensing method can be found in Figure 1-8 as sketched by Wild *et al.*, specifically methods using (a) evanescent field couplers, (b) fused tapered couple, (c) frustrated total internal refraction, (d) lateral misalignment, (e) Ronchi gratings, and (f) microbending.

The coupling ratio of evanescent field couplers depends on the distance between

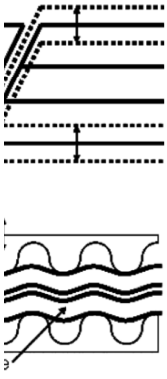

tapered couple; (c)
ıd (f) microbending.
d couple, the arrow

two fibers and the refractive index of the material separating the fibers. Therefore, the coupling ratio can be modulated as a function of these two parameters and has been successfully demonstrated as an acoustic sensor by [27]. A multimode variation of that design was presented by [28]. A schematic of the sensor is shown in Figure 1-8 (a).

The fused tapered couple approach is a more recent adaptation of the original evanescent field coupler approach. This method takes advantage of the fact that an incident strain field varies the length of the fused-tapered coupling region and thereby changes the coupling ratio. Work in this area has been carried out by Chen *et al.* [29–31] , and a schematic of the sensor is shown in Figure 1-8 (b).

Spillman and McMahon [32] have developed a sensor based on the method of frustrated total internal refraction; it is intensity-based and depends on the acoustically modulated lateral separation between two angled fiber tips. Phillips [33] has demonstrated a similar approach where instead of lateral distance modulation, the refractive index outside of the fiber is modulated by an acoustic field resulting in changes of detectable reflected intensity. A schematic of the sensor is shown in Figure 1-8 (c).

Spillman and Gravel [34], as well as Rines [35] have developed sensors based on lateral fiber misalignment between a fixed and a simply supported fiber. An acoustic field induces misalignment by oscillating the simply supported fiber; the resulting intensity modulation is measured. A schematic of the sensor is shown in Figure 1-8 (d).

Spillman [36], Spillman and McMahon [37], and Tietjen [38]demonstrated hydrophones based on Schlieren intensity modulation. Their sensor is composed of two Ronchi gratings that are located perpendicular to the optical axis of two longitudinally aligned fibers as shown in Figure 1-8 (e). One grating is connected to a diaphragm and

thus responds to acoustic pressure by modulating in the grating direction which results in a change of intensity detected by the optical system.

Fields *et al.* [39] demonstrated an intensity based sensor based on attenuation generated by various degrees of induced microbending. A multimode fiber is located between two ridged plates as shown in Figure 1-8 (f); applied external force causes the fiber radii to decrease, causing increased attenuation and thereby modulating the output intensity. Similar work is presented by Fields and Cole [40] and Lagakos *et al.* [41,42].

1.2.2 Sound Localization with Sensor Arrays

The purpose of sound localization is to detect a position of acoustic disturbance in two or three dimensions. Applications for sound localization include hearing aids, targeting systems, gunshot localization, search and rescue applications, as well as autonomous robot navigation; all of these applications benefit from a reduced sensor size. Reducing the size makes the sensor more portable, versatile, cheaper, and more environmentally friendly. In addition to these benefits, microscale arrays are capable of operating in the near field, which, due to the large microphone separation, is impossible for macroscale devices that have been designed utilizing the plane wave assumption [48]. The plane wave assumption is common, since it simplifies data evaluation significantly; when the separation distance, d, between a microphone pair is much smaller than the distance, l, between the sound source and the array, the plane wave assumption is satisfied. Microscale arrays overcome the near field limitation since the separation distance between the microphones is small relative to the curvature of the acoustic wave-front [49]. Therefore, designing small sound localization arrays utilizing inexpensive, high performance ultraminiature microphones is important.

Current sound localization techniques tend to utilize very large microphone arrays to maximize the time difrence of arrival (TDOA) between different pairs of microphones; a large TDOA allows for a greater spatial localization resolution [50]. Triangulation methods, similar to ones used in seismological earthquake localization, are employed to extract useful information from the TDOA data [51]. Therefore, the challenge of small scale microphone arrays is poor accuracy due to almost indistinguishable TDOA values between microphone pairs. To address the fundamental challenge of reducing the inter-microphone-pair-distance without reducing the TDOA, several authors have turned to biomimetic designs based on fly ears [52–57]. While the sensor presented in this work cannot be utilized in functional arrays that challenge size to performance ratio of the fly ear inspired microphones, it does have strong potential for high performance arrays made up of a large number of microphones.

1.3 Objective and Scope of Thesis Work

The primary objective of this thesis is to design, fabricate, and characterize a ultra-miniature fiber optic acoustic pressure sensor, and to study an microphone array constructed with these sensors for sound source localization. The sensor should meet the following requirements:

i) it can be fabricated inexpensively via a batch process,

ii) the sensor performance characteristic should be able to be easily tailored for various application needs,

iii) the sensor should have excellent performance in terms of bandwidth, sensitivity, and signal-to-noise ratio, despite of its small size.

1.4 Thesis Organization

The rest of the thesis is organized as follows. In Chapter 2, the sensor is introduced. Modeling, designed and fabrication of the sensor are discussed. The optical interrogation subsystem is introduced at the end of the chapter. In Chapter 3, the sensor system is characterized experimentally. Discrepancies between the theoretical and actual performance of the sensor are examined. Sound localization via a three sensor array is discussed in Chapter 4, and experimental results are shown. In Chapter 5, the dissertation work is summarized, and future work is addressed. Relevant simulation codes are included in the Appendix.

2 Sensor Development

2.1 Introduction

The miniature polymer diaphragm based fiber optic microphone developed in this thesis is composed of

i) a polymer diaphragm

ii) a silica sensor housing structure that couples the diaphragm with

iii) an optical fiber that connects to an optical interrogation subsystem.

Assembled, these components form a low-finesse Fabry-Pérot sensor. The working principle was discussed in Section 1.2.1.

In this chapter, the sensor diaphragm modeling and design will be discussed first. Subsequently, the newly developed batch-compatible procedure for polymer diaphragm fabrication and assembly is detailed. Finally, the optical interrogation subsystem technique is discussed.

2.2 Sensor Design and Modeling

2.2.1 Sensor Design

The ferrule-based design of the microphone was chosen to facilitate easy cavity length adjustments; the cavity length is critical to the sensitivity of the sensor. The dimensions of the ferrule were chosen to fit a standard single mode fiber. Selecting a housing ferrule determines the diameter of the transduction membrane, which is the most influential component of a microphone pertaining to its performance. The membrane determines important performance aspect such as bandwidth and sensitivity and can be

designed by varying the diaphragm material, thickness, and diameter. The diaphragm material should have the following properties:

i) good optical properties compatible with the optical interrogation subsystem,

ii) good mechanical properties so that large dynamic fluctuations can be obtained even with a small stimulus, and

iii) properties favorable to microscale fabrication requirements.

The cross-sectional schematic of a fully assembled sensor element is shown in Figure 2-1. It consists of a capillary tube, a single-mode fiber, and a semi-permeable UV polymer diaphragm. The diaphragm can be modeled as an edge-clamped circular plate. The analytical static state solution for obtaining the deflection of the diaphragm center is well known and can be calculated as a function of the applied pressure change, ΔP, given the mechanical and dimensional properties of the diaphragm. The static center deflection, ΔX [9,58], can be calculated using:

$$\Delta X = \frac{3\left(1-\nu^2\right)a^4}{16Ed^3}\Delta P \quad , \tag{2.1}$$

where a and d are the diaphragm radius and thickness, respectively as indicated in Figure 2-1. E represents the Young's modulus of the diaphragm polymer and υ its Poisson's ratio. The polymer chosen for membrane fabrication has a Young's modulus (21 MPa) more than 8000 times smaller than silicon (185 GPa). This property, in addition to other properties that allow for uniform, nanometer-scale thickness control allow the diaphragm to retain a high sensitivity to acoustic pressure perturbations even with a small diameter. An additional benefit of the diaphragm's low Young's modulus is the expected spontaneously recession of the diaphragm inside the capillary tube as shown Figure 2-1

nt.

in and denoted by *r*. This protects the diaphragm from damage and increases the tension of the diaphragm, resulting in a higher first resonant frequency and consequently a larger sensor bandwidth. In addition, the expected diaphragm permeability to air due to the small thickness of the membrane will increase the damping of the microphone and reduce the undesired effect of the first resonant frequency.

The diaphragm polymer has a refractive index equal to that of an optical fiber core, which is selected to be suitable for use with the proposed optical interrogation system. The two-beam interferometric optical system produces the largest signal visibility when the intensities of the two reflected beams are equal. Matching the refractive indices of the fiber core and the diaphragm polymer results in approximately equal beam intensities. In terms of fabrication compatibility, the polymer exhibits

hydrophilicity and low viscosity, enabling it to form thin films of uniform thickness by spreading quickly and evenly across water surfaces. Diaphragm uniformity ensures the optimal modal response and reflectivity. Finally, the polymer is UV curable. The use of UV polymer is especially important because of its intrinsic properties that completely solidify the polymer with the exception of a thin layer where the polymer is exposed to air when it is exposed to UV light. This uncured layer is used in the fabrication process to fix the diaphragm to polished endface of the glass capillary that serves as the sensor housing. Fixing the diaphragm to the glass capillary requires strong adhesion without a reduction in tension over time to ensure constant performance over a long lifecycle.

2.2.2 Sensor Diaphragm Modeling

The dynamic response of a clamped circular membrane was modeled in order to predict the feasibility of the sensor.

Free Vibration

The governing equation for free vibration is

$$\rho h \frac{\partial^2 w}{\partial t^2} + \frac{D}{a^4}\nabla^4 w - \frac{N_0}{a^2}\nabla^2 w = 0 \quad , \tag{2.2}$$

where ρ, h, a, and N_0 are defined as density, thickness, radius, and initial tension per unit area, respectively; $D=Eh^3/12/(1-\nu^2)$ is the flexural stiffness with E and ν representing the Young's modulus and Poisson's ratio respectively.

The boundary conditions of the diaphragm are

$$\begin{cases} w(r,\theta,t)\big|_{r=0} < \infty \\ w(r,\theta,t)\big|_{r=1} = 0 \\ \left.\dfrac{\partial w(r,\theta,t)}{\partial r}\right|_{r=1} = 0 \\ w(r,\theta+2\pi,t) = w(r,\theta,t) \end{cases}. \tag{2.3}$$

Assuming that the displacement is in the form of

$$w(r,\theta,t) = U(r)\Theta(\theta)e^{j\omega t} \tag{2.4}$$

Substituting (2.4) into (2.3) yields

$$\nabla^4\left[U(r)\Theta(\theta)\right] - \frac{N_0 a^2}{D}\nabla^2\left[U(r)\Theta(\theta)\right] - \frac{\rho h a^4}{D}\omega^2\left[U(r)\Theta(\theta)\right] = 0. \tag{2.5}$$

However, (2.5) can be rewritten as either

$$\left(\nabla^2 - \alpha_1^2\right)\left[U(r)\Theta(\theta)\right] = 0 \tag{2.6}$$

or

$$\left(\nabla^2 + \alpha_2^2\right)\left[U(r)\Theta(\theta)\right] = 0, \tag{2.7}$$

where

$$\alpha_1^2 = \frac{1}{2}\left(\sqrt{\chi^2 + \frac{4\rho h a^4}{D}\omega^2} + \chi\right), \tag{2.8}$$

$$\alpha_2^2 = \frac{1}{2}\left(\sqrt{\chi^2 + \frac{4\rho h a^4}{D}\omega^2} - \chi\right), \tag{2.9}$$

$$\text{and } \chi = \frac{N_0 a^2}{D}. \tag{2.10}$$

α_1 and α_2 are related by

$$\alpha_1^2 = \alpha_2^2 + \chi. \tag{2.11}$$

Separating the variables in (2.6) and (2.7) results in

$$\frac{\frac{1}{r}\frac{\partial U(r)}{\partial r}+\frac{\partial^2 U(r)}{\partial r^2}-\alpha_1^2 U(r)}{\frac{1}{r^2}U(r)}=-\frac{\frac{\partial^2\Theta(\theta)}{\partial\theta^2}}{\Theta(\theta)} \tag{2.12}$$

and

$$\frac{\frac{1}{r}\frac{\partial U(r)}{\partial r}+\frac{\partial^2 U(r)}{\partial r^2}+\alpha_2^2 U(r)}{\frac{1}{r^2}U(r)}=-\frac{\frac{\partial^2\Theta(\theta)}{\partial\theta^2}}{\Theta(\theta)} \tag{2.13}$$

.

The angular part can therefore be obtained as

$$\Theta_m(\theta)=\begin{cases}\dfrac{1}{\sqrt{2\pi}} & m=0\\ \dfrac{1}{\sqrt{\pi}}\cos m(\theta-\varphi_m) & m=1,2,\mathrm{L}\end{cases}, \tag{2.14}$$

which satisfies

$$\int_0^{2\pi}\Theta_m(\theta)\Theta_n(\theta)\,d\theta=\delta_{mn}. \tag{2.15}$$

Equations (2.12) and (2.13) can be rewritten in the forms of Bessel functions:

$$\frac{\partial^2 U(r)}{\partial r^2}+\frac{1}{r}\frac{\partial U(r)}{\partial r}-\alpha_1^2 U(r)=\frac{m}{r^2}U(r) \tag{2.16}$$

or

$$\frac{\partial^2 U(r)}{\partial r^2}+\frac{1}{r}\frac{\partial U(r)}{\partial r}+\alpha_2^2 U(r)=\frac{m}{r^2}U(r) \tag{2.17}$$

.

Considering the boundary condition in the first equation of (2.10), the solution of $U(r)$ can be assumed in the following general form:

$$U(r) = A_{1m} I_m(\alpha_1 r) + A_{2m} J_m(\alpha_2 r), \tag{2.18}$$

where the second kind form of Bessel function and modified Bessel function are excluded. Substituting (2.18) into the boundary conditions expressed in (2.3) yields

$$A_{1m} I_m(\alpha_1) + A_{2m} J_m(\alpha_2) = 0 \tag{2.19}$$

and

$$\alpha_1 A_{1m} I_m'(\alpha_1) + \alpha_2 A_{2m} J_m'(\alpha_2) = 0. \tag{2.20}$$

Eliminating A_{1m} and A_{2m} gives

$$\alpha_1 I_m'(\alpha_1) J_m(\alpha_2) + \alpha_2 I_m(\alpha_1) J_m'(\alpha_2) = 0. \tag{2.21}$$

For a given m, α_1 and α_2 can be solved from (2.21) and (2.11) as α_{1mn} and α_{1mn}, from which we can get the natural frequencies:

$$\omega_{mn} = \sqrt{\frac{D}{\rho a^4 h}\left(\alpha_{2mn}^4 + \alpha_{2mn}^2 \chi_{tp}\right)} = \lambda \alpha_{1mn} \alpha_{2mn}, \tag{2.22}$$

where

$$\lambda = \sqrt{\frac{D}{\rho h a^4}} = \sqrt{\frac{\kappa}{m}} \tag{2.23}$$

with

$$\kappa = \frac{\pi D}{a^2}, \tag{2.24}$$

$$m = \pi a^2 h \rho. \tag{2.25}$$

The mode shape functions are:

$$U_{mn}(r) = \frac{1}{\sqrt{C_{mn}}}\left[I_m(\alpha_{1mn}) J_m(\alpha_{2mn} r) - J_m(\alpha_{2mn}) I_m(\alpha_{1mn} r)\right], \tag{2.26}$$

where C_{pmn} is the coefficient chosen to normalize the mode shape as follows

$$\int_0^1 U_{ij}(r)U_{mn}(r)rdr = \delta_{im}\delta_{jn} \quad (2.27)$$

Forced Vibration

The governing equation for forced vibration is

$$\rho h\frac{\partial^2 w}{\partial t^2} + \mu\frac{\partial w}{\partial t} + \frac{D}{a^4}\nabla^4 w - \frac{N_0}{a^2}\nabla^2 w = f \quad (2.28)$$

Assuming the external pressure, *f*, is in the form

$$f(r,\theta,t) = \sum_{m,n} F_{mn}U_{mn}(r)\Theta_m(\theta)e^{j\omega t} \quad (2.29)$$

and the response of the plate is

$$w(r,\theta,t) = \sum_{m,n} W_{mn}U_{mn}(r)\Theta_m(\theta)e^{j\omega t} \quad (2.30)$$

Substitute (2.29) and (2.30) into (2.28) yields

$$\begin{aligned}&\sum_{m,n}\left\{W_{mn}\left[\left(-\rho_p h_p\omega^2 + \mu j\omega\right) + \frac{D}{a^4}\nabla^4 - \frac{N_0}{a^2}\nabla^2\right]U_{mn}(r)\Theta_m(\theta)\right\}\\ &= \sum_{m,n}\left\{F_{mn}U_{mn}(r)\Theta_m(\theta)\right\}\end{aligned} \quad (2.31)$$

From (2.5) we have:

$$\left(\frac{D}{a^4}\nabla^4 - \frac{N_0}{a^2}\nabla^2\right)U_{mn}(r)\Theta_m(\theta) = \rho_p h_p\omega_{mn}^2 U_{mn}(r)\Theta_m(\theta) \quad (2.32)$$

Hence, (2.31) can be reformed as:

$$\sum_{m,n}\left\{\left[W_{mn}\left(-\rho h\omega^2 + \mu j\omega + \rho h\omega_{mn}^2\right) - F_{mn}\right]U_{mn}(r)\Theta_m(\theta)\right\} = 0 \quad (2.33)$$

Utilizing the orthogonality of the mode functions (2.15) and (2.27) yields

$$\frac{W_{mn}}{F_{mn}} = \frac{1}{\rho h\left(-\omega^2 + 2\xi\omega_{mn}j\omega + \omega_{mn}^2\right)} \quad (2.34)$$

where $\xi_{mn} = \mu / \left(2\rho_p h_p \omega_{mn} \right)$ is the defined damping factor.

Equation (2.41) can also be written as

$$\frac{W_{mn}}{F_{mn}} = \frac{\pi a^2}{\kappa \left(\alpha_{1mn} \alpha_{2mn} \right)^2 \left[1 - \left(\frac{\omega}{\omega_{mn}} \right)^2 + 2\xi_{mn} j \frac{\omega}{\omega_{mn}} \right]}. \tag{2.35}$$

Resonance Frequency and Sensitivity

The material properties of the polymer chosen for its desirable fabrication characteristics are:

- Young's modulus: E = 20.7 MPa
- Poisson's ratio: ν = 0.4
- Density: ρ = 1.1×10^3 kg/m^3

When the in-plane tension is small, the diaphragm can be modeled as a pure plate, whose first natural frequency is equal to

$$f_1 = \frac{\alpha_{101} \alpha_{201}}{2\pi} \sqrt{\frac{E}{12\left(1-\nu^2\right)\rho_s}} \frac{h}{a^2} = 70251 \frac{h}{a^2} kHz, \tag{2.36}$$

where the thickness, h, and radius, a, are in the units of μm.

In order to adjust the first natural frequency to be at 20 kHz, h and a should satisfy

$$\frac{a^2}{h} = 3513. \tag{2.37}$$

Due to the small scale of the sensor, it is reasonable to assume that the pressure is uniform across the membrane surface. The static sensitivity in terms of center displacement per unit pressure is therefore given by

$$\frac{w(r=0)}{p_0} = \frac{a^4}{64D} = \frac{3(1-\nu^2)}{16E}\frac{a^4}{h^3} = 7.61\times10^{-6}\frac{a^4}{h^3} nm/Pa \quad , \tag{2.38}$$

where the thickness, h, and radius, a, have the units of μm.

It has been shown that with optical detection technique, the minimum detectable diaphragm displacement is on the order of 0.1 nm. h and a should therefore satisfy

$$\frac{a^4}{h^3} = \frac{13141}{p_0} \quad . \tag{2.39}$$

Combining (2.37) and (2.39) gives the combination of geometric parameters of the polymer microphone for various minimum detectable sound pressure levels.

Table 2-1. Combinations of thickness and radius to satisfy the design requirements

SPL (dB)	p_0 (Pa)	a (μm)	h (μm)
0	0.00002	8.12	0.019
5	3.56E-05	10.83	0.033
10	6.32E-05	14.45	0.059
15	0.000112	19.26	0.106
20	0.0002	25.69	0.188
25	0.000356	34.25	0.334
30	0.000632	45.68	0.594
35	0.001125	60.91	1.056

Among all the possible combinations listed in Table 2-1, the values chosen for the design parameters are a = 45 μm, and h = 0.6 μm because fabrication of that combination is feasible. The fundamental frequency is calculated to be 20.82 kHz. The dynamic

response and sensitivity are shown in Figure 2-2 and Figure 2-3, respectively.

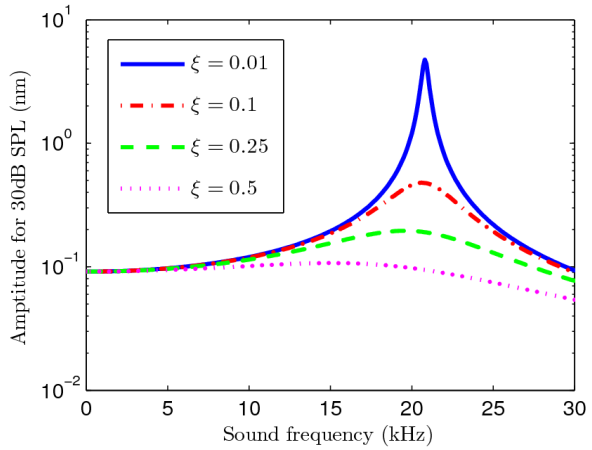

Figure 2-2. Dynamic response of a clamped circular membrane (radius: 45 μm, thickness: 0.6 μm)

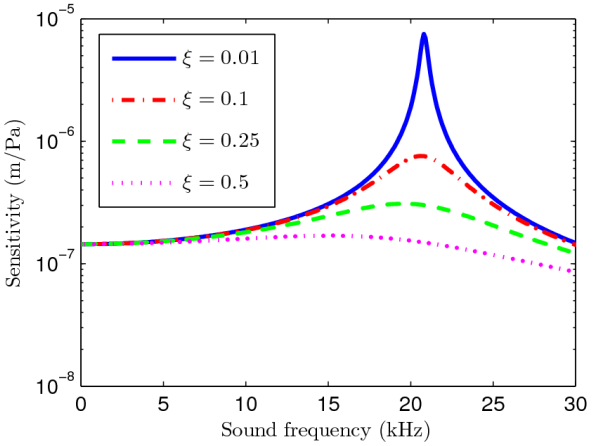

Figure 2-3. Sensitivity of a clamped circular membrane (radius: 45 μm, thickness: 0.6 μm)

Sensor Design with Consideration of Cost and Ease of Fabrication

To reduce the cost of the sensor, the most commonly used single mode fiber (SMF), i.e., Corning's SMF-28e, is selected. Its cladding diameter is 125.0 ± 0.7 μm which requires complex processes such as UV molding, fiber etching, or custom ferrule fabrication to achieve a diaphragm diameter of 45 μm as proposed in the previous section. Furthermore, from a fabrication perspective, UV molding and fiber etching do not provide the flexibility to easily adjust the cavity length of the sensor. The easiest

method of fabricating a sensor would be to fix a diaphragm to the housing structure and then to insert and fix an optical fiber at the desired cavity length. Given that fabrication scheme, the diaphragm must be slightly larger than the diameter of the optical fiber. To facilitate easy and inexpensive fabrication, the sensor housing must by cylindrical and capable of fitting over a standard SMF-28e fiber with reasonable clearance. The sensor housing must be able to form a strong adhesive bond with UV curable polymer for bonding purposes. To ensure that the optical fiber is perpendicular to the diaphragm as shown in Figure 2-1, the housing should be fabricated from a material with crystal lattices that enable cleaving to form smooth facets perpendicular to the cylindrical axis of the housing. Finally, the housing must be rigid enough to withstand axial deformation through acoustic pressure waves. All of these requirements are fulfilled by using glass capillary tubes (TSP150375 from Polymicro Technologies). The inner diameter of the tube is 150 μm, which allows for 25 μm of clearance when the fiber is inserted. The wall thickness is large enough (105 μm) to withstand large acoustic sound pressures without deformation, while being thin enough to facilitate cleaving. The Young's modulus and thermal coefficient are the same as the optical fiber, which alleviates unwanted effects, such as thermal expansion. While this design increases the size of the sensor, it reduces the cost and complexity of fabrication while increasing the sensitivity as indicated by Equation (2.1).

A parametric study was carried out to investigate the performance of a sensor with a 150 μm diaphragm. The thickness and first natural frequency are calculated using (2.39) and (2.36) respectively, given that the optical system is capable of detecting a deflection on the order of 0.1 nm.

Table 2-2. Combinations of thickness and SPL given a fixed radius

SPL (dB)	p_0 (Pa)	h (μm)	f_0 (kHz)
0	0.00002	0.364	4.55
5	3.56E-05	0.441	5.51
10	6.32E-05	0.534	6.67
15	0.000112	0.646	8.07
20	0.0002	0.784	9.79
25	0.000356	0.950	11.86
30	0.000632	1.150	14.36
35	0.001125	1.394	17.41
40	0.002	1.689	21.09

Table 2-2 clearly shows the tradeoff between sensitivity and bandwidth; as the minimum detectable sound pressure increases which is equivalent to a decrease in sensitivity, the

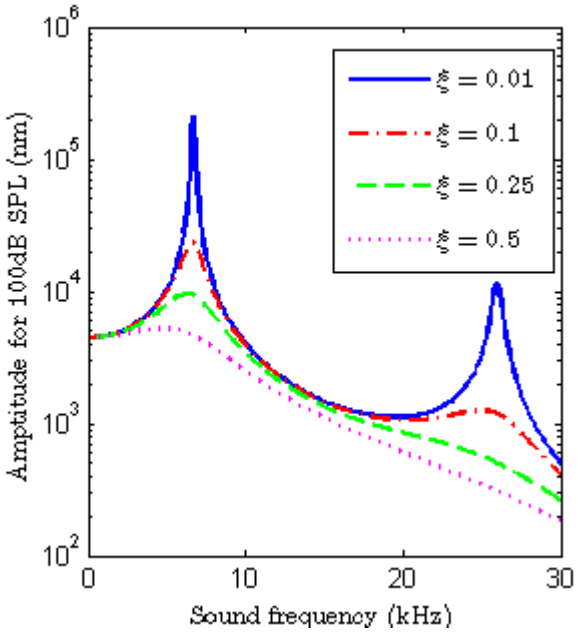

Figure 2-4. Dynamic response of a clamped circular membrane (radius: 75 μm, thickness: 0.534 μm)

first natural frequency increases, expanding the bandwidth of the sensor. To give an example of the level of SPL, a calm room is generally characterized as having a SPL of 20 – 30 dB. Any combination of *a* and *h* producing a minimum detectable SPL larger than 30 dB would not yield a sensor with a reasonable sensitivity. From the remaining

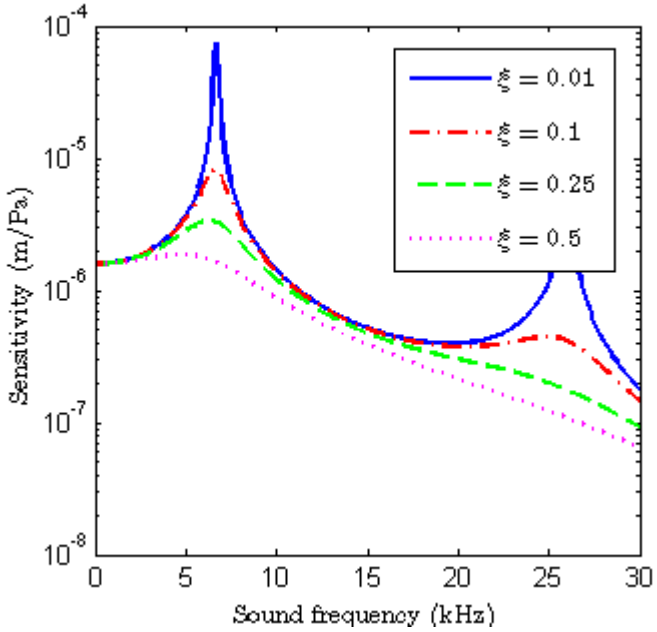

Figure 2-5. Sensitivity of a clamped circular membrane (radius: 75 μm, thickness: 0.534 μm)

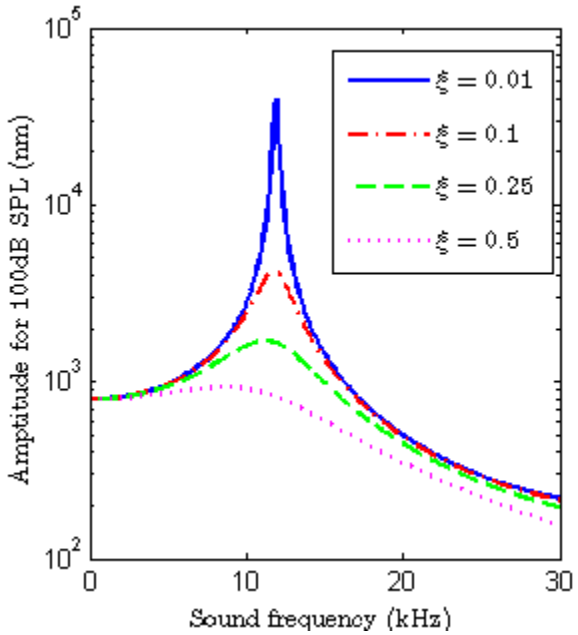

Figure 2-6. Dynamic response of a clamped circular membrane (radius: 75 μm, thickness: 0.950 μm)

combinations, 10 dB and 25 dB SPL were chosen for further examination. The dynamic response and sensitivity are shown in Figure 2-3 and Figure 2-4 for 10 dB SPL; Figure 2-5 and Figure 2-6 show the same information for 25 dB SPL minimum detectable sound pressure. The figures and Table 2-2 indicates that none of the designs, assuming

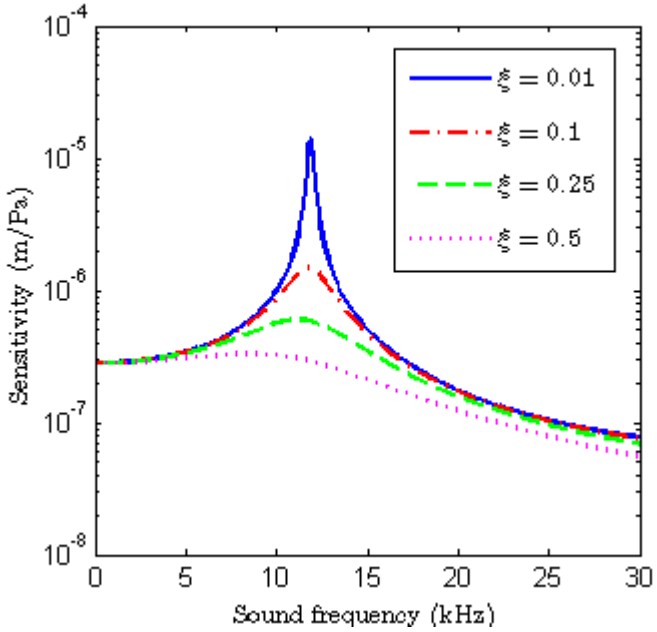

Figure 2-7. Sensitivity of a clamped circular membrane (radius: 75 μm, thickness: 0.950 μm)

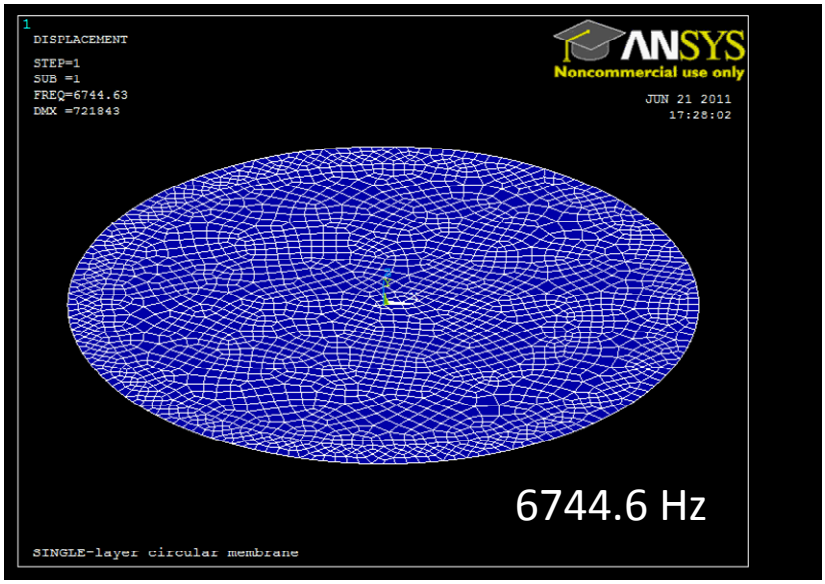

Figure 2-8. ANSYS model results verify MATLAB model

negligible radial diaphragm tension, will produce a sensor with a flat response large enough to cover the entire bandwidth of human hearing from 20 Hz to 20 kHz. One possible solution would be to design a diaphragm with a large damping ratio, ξ, by

mechanically or chemically introducing uniform pores in the diaphragm.

The Matlab code used for the simulations in this subsection can be found in Appendix A.

ANSYS Modeling

The previous model was verified with an ANSYS model. All ANSYS model codes can be found in Appendix B. Figure 2-7 shows the meshed, 150 μm diameter and 540 μm thick, diaphragm modeled. The ANSYS model was also used to determine the deflection of the diaphragm depending on the magnitude of the impinging sound wave as shown in Figure 2-8. Results indicate that the deflection should be detectable by the interrogation system at the lower design specified sound pressure level of 20 dB.

2.3 Sensor Fabrication

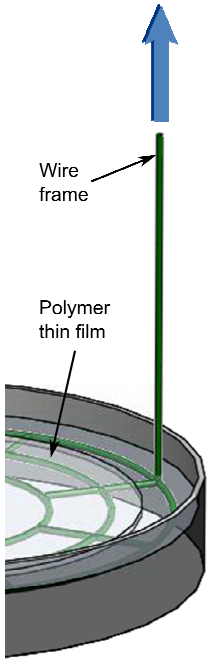

t and (b) schematic

2.3.1 Sensor Diaphragm Fabrication

The diaphragm is fabricated by dispensing a 1 mm^3 droplet of polymer (OP-4-20641 from DYMAX Corp.) onto the center of a room temperature distilled water surface contained within a plastic petri dish with a 150 mm diameter. The uniformity of the diaphragm achieved in this fashion is exceptional and the thickness can be adjusted by varying the polymer volume. The diaphragm is then pre-cured for 5-8 minutes using low-powered UV light to form a highly viscous polymer layer that can be lifted off the water.

2.3.2 Sensor Assembly

The fabrication process of the pressure sensor is compatible with batch fabrication and can be summarized by the following steps. First, multiple glass tubes (TSP150375 from Polymicro Technologies) are cleaved to the same length. The protective polymer covering the tubes is burned off and both endfaces are polished to ensure orthogonal and smooth surfaces. The tubes are sonically cleaned to remove burn residue. Next, the array of tubes is inserted into a porous foam substrate as shown in Figure 2-9 (b). Extrusion height and parallelism of each tube are matched to ensure that all tubes puncture the diaphragm simultaneously when it is applied.

A custom wire frame as shown in Figure 2-9 (b) is used to apply the diaphragm to an array of glass tubes by simultaneously lowering the tube substrate and lifting up the diaphragm with the wire frame structure. Immediately after application to the glass tubes, the viscous polymer layer is recessed a distance, *r*, as shown in Figure 2-9 (a), into the glass tube due to capillary forces. The distance, *r*, was measured using a white light topography measurement system (TMS-1200 by Polytec). The result is shown in the Chapter 3. Once applied, the polymer layer is post-cured using UV light to ensure proper adhesion to the glass tube. Due to polymer shrinkage during the curing process and the capillary force recessing the diaphragm, membrane tension increases. However, due to the viscous nature of the diaphragm at the time of application, the tension reduces the thickness of the diaphragm.

Finally, in order to form a functioning Fabry-Pérot sensor element, a bare, cleaved, single mode fiber is inserted into the glass tube using a high precision 3-axis mechanical stage (NanoMax-TS, MAX303 by Thorlabs). The cavity length, L_s, as shown

in Figure 2-9, can be adjusted to match the requirements of the optical interrogation subsystem. The cavity length for the research presented in this publication was chosen to be 60 μm. Easily adjusting *L* is a distinct advantage over smaller, fiber-sized sensor heads [8,43,59,60] where cavity length adjustment is tedious and difficult to control. Once the fiber is in place, a small drop of UV polymer is used to secure the sensor housing to the fiber. Only a small amount of glue is applied so that a pressure port is maintained as shown in Figure 2-9 (b). The pressure port is intended to increase the damping of the diaphragm by only providing air exchange through a small opening. In addition, dynamic pressure measurements are plausible even in high pressure environments, since the air cavity inside the sensor can quickly self-regulate. This expands the area of application for this sensor while protecting the diaphragm from bursting. Finally, providing a pressure port alleviates potential problems during the fabrication process that could cause the diaphragm to rupture or deform to such a degree that the performance of the sensor is seriously compromised.

2.4 Sensor Interrogation System

The low-coherence fiber-optic interferometry (LCFOI) sensor interrogation system presented in this section has not been developed as part of this thesis; it is included for the sake of presenting the complete system used to characterize the performance of the sensor. The advantages of the system are primarily low cost due to the integration of a broadband light source instead of a more expensive single-frequency laser and low wavelength instability effects as the Optical Path Difference (OPD) can be very small. Small OPD is also desirable for the sake of sensor miniaturization.

ometer

A configuration of the most commonly used fiber-optic low coherence interferometer based on two interferometers is shown in Figure 2-10. A broadband light source with coherence length L_c is guided into a fiber coupler before entering the *sensor interferometer*. The output from the sensor interferometer is then transferred via fiber link to the *reference interferometer*, which, given the condition that the sensing OPD, L_s, is much shorter than the coherence length, L_c, of the light source such that under normal conditions there is no interference effect, has the purpose of reestablishing the interference effects from the temporally incoherent output of the sensor interferometer. The reestablished interference effects can be detected by a conventional photodecector.

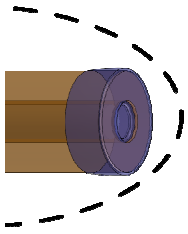

2.4.1 LCFOI Configuration

The specific system used in this work is shown in Figure 2-11. Light from the low coherence superluminescent diode (SLD) light source (OELED-100 by O/E Land Inc., P_{out} = 99.7 μW, λ_c = 1317.8 nm, $\Delta\lambda_{FMHW}$ = 42 nm) with a coherence length L_c traveling towards the sensing interferometer is reflected first by the fiber endface (~4%) and then by the diaphragm (~4%). The electric vectors of the light, E_1 and E_2, of both reflected beams can are expressed by Equations (2.40) and (2.41), respectively.

$$E_1(\omega t, \phi) = A_1(\omega t)e^{(j\phi)} \tag{2.40}$$

$$E_2(\omega t, \phi) = A_2(\omega t)e^{(j(\phi - k_0 L_s))} \tag{2.41}$$

where A, ω, and □ represent the amplitude, frequency, and phase of the electric field, respectively. The imaginary unit is represented by j, t represents time, and L_s indicates the length of the sensing cavity. The free-space wavenumber, k_0, is equal to $(2\pi)/\lambda$ where λ is the wavelength. The reflected beams have an OPD of L_s that induces a phase difference $\phi_s = k_0 L_s$ and the acoustic pressure induced diaphragm deflection produces a phase difference change $\Delta\phi$ in ϕ_s. Next, both reflected beams enter the reference cavity (FFP-TF2 by Micron Optics), which has an initial optical path difference L_s, or phase difference $\phi_r = k_0 L_r$. As a result of the path imbalance, L_r, four electric field vectors exit the reference cavity as expressed by Equations (2.42) – (2.45).

$$E_{11}(\omega t, \phi) = A_{11}(\omega t)e^{(j(\phi))} \tag{2.42}$$

$$E_{12}(\omega t, \phi) = A_{12}(\omega t)e^{(j(\phi - k_0 L_r))} \tag{2.43}$$

$$E_{21}(\omega t, \phi) = A_{21}(\omega t)e^{(j(\phi - k_0 L_s))} \tag{2.44}$$

$$E_{22}(\omega t, \phi) = A_{22} e^{\left(j\left(\phi - k_0 |L_s - L_r|\right)\right)} \tag{2.45}$$

When the reference interferometer is phase-matched to the sensing interferometer ($L_r \cong L_s$) and the coherence length $L_c << L_r$, L_s, the output intensity received by the photodetector (Model 2011 by New Focus) can be simplified using [61] to Equation (2.46).

$$I_{out} \approx I_0 + I_{ac} \cos k_0 (L_s - L_r) = I_0 + I_{ac} \cos(\phi_s - \phi_r) = I_0 + I_{ac} \cos(\Delta\phi) \tag{2.46}$$

where I_0 is the intensity of the low coherence light source, I_{ac} is the constant related to the mirror properties of the FP interferometer, and $\Delta\phi$ is the differential phase change between the sensing interferometer and reference interferometer. Note that $\Delta\phi$ is the only parameter related to the center displacement, X, of the microphone diaphragm and $\Delta\phi = 2k_0 X$. Therefore, the pressure sensitivity (displacement/pressure) of the diaphragm can be amplified by a factor of $2k_0$ (107 times at λ=1300 nm). The reference cavity length, L_r, is held constant and fine-tuned to fulfill the interference conditions using a DC voltage.

2.5 Summary

A polymer is selected based on mechanical and optical properties that enable integration with the optical system. Simulation results suggest that the mechanical properties are sufficient to enable miniaturization of an acoustic sensor while maintaining high sensitivity and bandwidth. Based on

i) simulation results that suggest good performance and diaphragm deflections in a range detectable by the proposed optical interrogation system,

ii) inexpensive materials,

iii) and material compatibility with a novel batch fabrication procedure,

a sensor with a 950 nm thick, 150 μm diaphragm diameter was designed.

3 Experimental Results

3.1 Introduction

The sensor described in the previous chapter was batch fabricated and characterized. All characterization experiments, when necessary, have been conducted in an anechoic chamber at the Army Research Laboratory.

3.2 Characterization of Sensor Diaphragm

Immediately after application to the glass tubes, the viscous polymer diaphragm layer is recessed a distance, *r*, as shown in Figure 2-9 (a), into the glass tube due to capillary forces. The distance, *r*, was measured using a white light topography measurement system (TMS-1200 by Polytec) and is shown in Figure 3-1. The Figure validates the 2.5 μm recession of the 960 nm thick diaphragm and the fact that the fabrication process yields a level diaphragm.

ıphragm.

lement

In addition to the TMS images, scanning electron microscope (SEM) images were taken to verify the porous nature of the diaphragm. A SEM picture of the finished sensing element is shown in Figure 3-2. Again, the recession of the diaphragm is clearly visible. However, the porous nature of the diaphragm is not visible at this low magnification. Highly magnified images of the diaphragm are shown in Figure 3-3. The image is taken at the housing-diaphragm boundary in order to demonstrate once more that the diaphragm is recessed; in the left image, the diaphragm is in focus and the capillary endface is not. The reverse situation is presented in the right image. The diaphragm, in addition to the

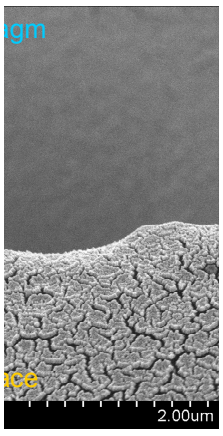

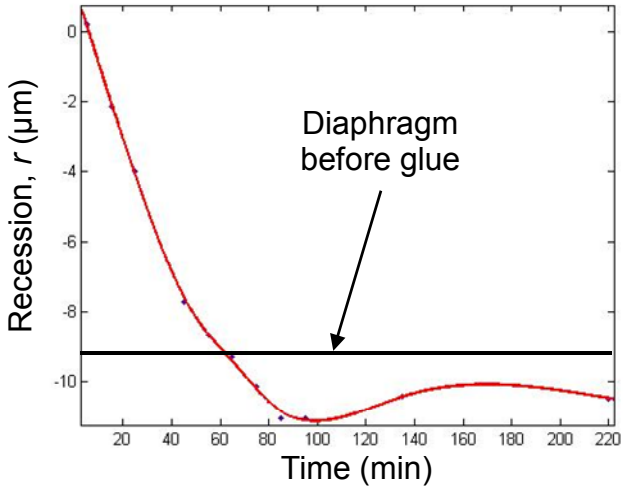

Figure 3-4. Effects of clogging the pressure port on the position of the diaphragm

recession, clearly exhibits nanoscale pores will increase the damping of the diaphragm and thus extend the bandwidth of the sensor even with a low first natural frequency.

Further examination of the diaphragm shows that clogging the pressure port results in initial outward bulging of the diaphragm as shown in Figure 3-4. The bulging is a result of the reduction of air cavity volume due to the encroaching UV polymer while retaining the same volume of trapped air. The UV polymer is driven by capillary forces. The permeable nature of the diaphragm allows air to escape slowly; the diaphragm recesses beyond the initial pre-glue position and never recovers to its original position due to the viscoelastic nature of the diaphragm. This can lead to severe performance degradation, since the sensor will likely not be operable at the system's quadrature point.

3.3 Sensor Performance Characterization

The sensor performance is highly tunable; the thickness and radius of the microphone diaphragm can be tailored to achieve optimal performance characteristics for

specific applications. The sensor characterized in this chapter has a 970 nm thick diaphragm and a diameter of 150 μm. The experimental setup is shown in Figure 3-5; the optical microphones being characterized are mounted directly to the reference microphone housing with the purpose of sampling the same pressure field simultaneously with both microphones. The reference microphone provides calibrated information of the pressure field at the location of the optical microphone. Due to the small size of the optical microphone, the pressure field is assumed to be equivalent at both microphone locations. Experiments conducted with various sensor mount rods of different diameters indicate that no significant degradation of the measured signal occurs as a result of rod or reference microphone induced sound wave distortion. The performance parameters characterized include the frequency response, dynamic range, bandwidth, resolution, and signal to noise ratio.

3.3.1 Frequency Response

Frequency response is the quantitative measure of the output spectrum of a system or device in response to a stimulus. The frequency response of the optical sensor is characterized by stimulating the reference and optical microphones at discrete sound

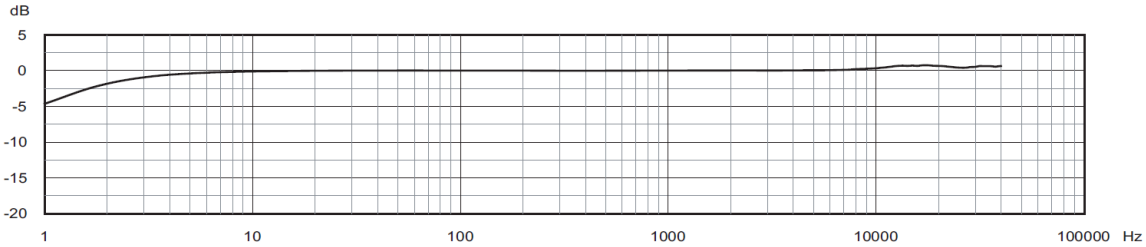

Figure 3-6. Frequency response calibration curve supplied by Brüel & Kjær for a type 4191 ½ inch free field condenser microphone [67].

frequencies in a range from 50 Hz to 20 kHz. The input pressure to the optical microphone is measured by the reference microphone. Given the known input and the output of the optical microphone, the transfer function, i.e. frequency response, can be calculated.

The reference microphone used to perform the calibration is a scientific condenser microphone (Brüel & Kjær 4191), which has a diaphragm diameter of ½ in. The manufacture provided frequency response curve of the reference microphone is shown in Figure 3-6, which exhibit a flat response between 10 Hz and 40 kHz. In comparison, the amplitude spectrum of the reference microphone as measured experimentally in the Army Research Lab's anechoic chamber is shown in Figure 3-7. The measurement entails 5000 logarithmically spaced data points at frequencies from 50 Hz to 20 kHz. The lower

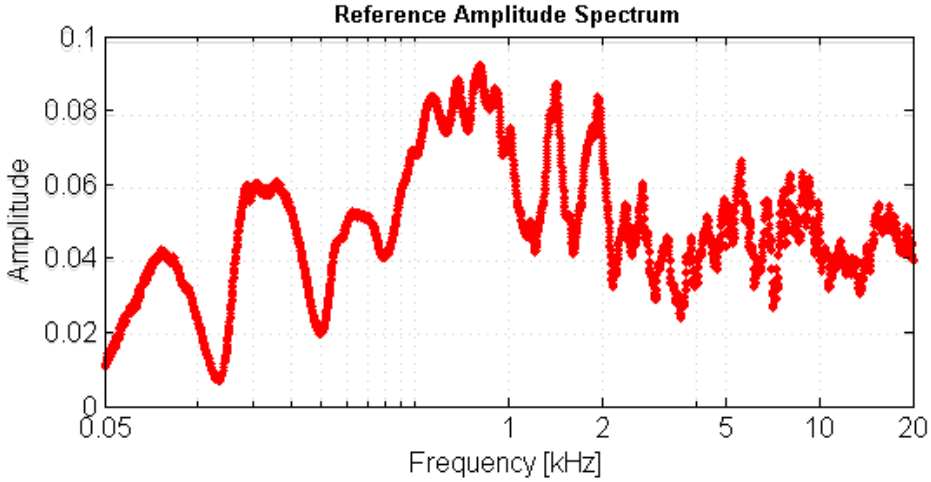

Figure 3-7. Brüel & Kjær ½ inch scientific condenser microphone amplitude spectrum.

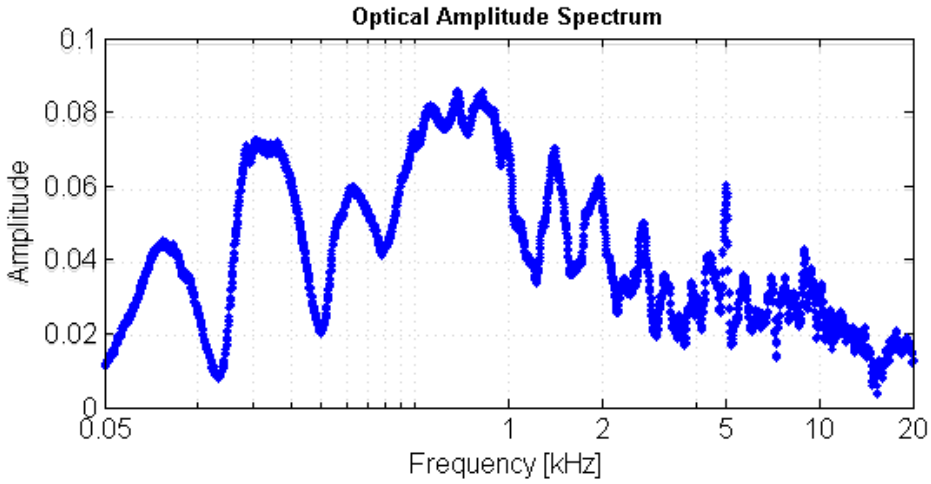

Figure 3-8. Optical microphone amplitude spectrum.

bound of the measurement is limited by the performance of the speaker. The performance of the speaker in combination with the measurement environment is responsible for the discrepancy between Figure 3-6 and Figure 3-7.

The obtained optical microphone amplitude spectrum is almost identical to that of the reference microphone. The optical microphone data was collected simultaneously with the reference data and is shown in Figure 3-8. Note that, similar to the reference

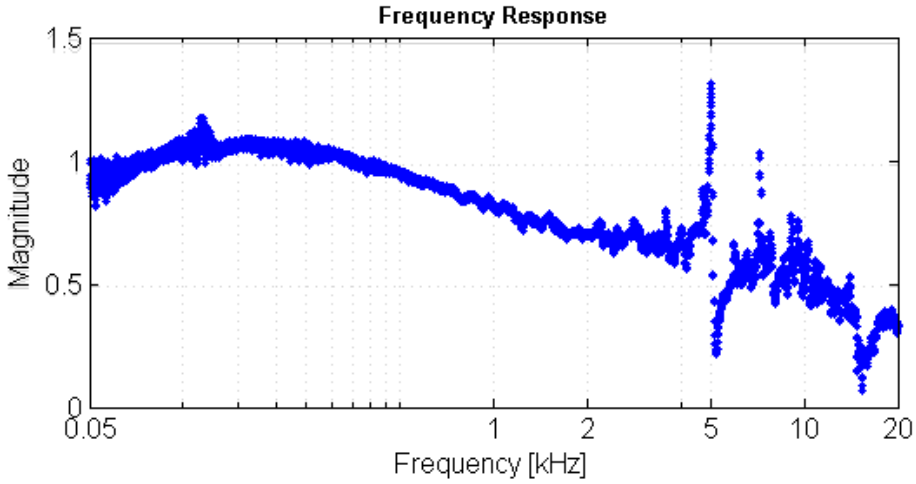

Figure 3-9. Frequency response of a miniature optical microphone with a 970 nm thick, 150 μm diameter diaphragm.

microphone, the amplitude spectrum is affected by the spectrum characteristic of the speaker as well as the measurement environment.

To determine the frequency response that represents the optical microphone's spectrum characteristic, the transfer function of the optical and reference microphones is calculated. The transfer function is shown in Figure 3-9; the data clearly exhibits a first natural frequency of ~ 5 kHz. Compared to the simulation data presented in Chapter 2, this result is much lower. To understand this discrepancy, the material properties and dimensions of the diaphragm, which are used to obtain the simulation result, need to be examined. All the material properties, except for the Poisson's ratio, are supplied by the vendor of the diaphragm material, while the diameter of the diaphragm can be easily measured. Thus, the most likely parameter to be the cause of the discrepancy between the simulation and the experiment is the diaphragm thickness. The diaphragm thickness was measured prior to its application to the capillary tubes due to the difficulty of measuring the suspended and recessed diaphragm thickness after sensor assembly. Since capillary action recesses the diaphragm during fabrication and curing results in polymer shrinkage, the thickness might well be reduced during sensor fabrication, which will result in a decrease in the natural frequency of the diaphragm.

Diaphragm Thickness Calibration

One plausible method of measuring the diaphragm thickness after assembly would be to insert an optical fiber with a translucent metal coating covering its endface to form a Fabry-Pérot cavity with the diaphragm. The metal layer is necessary to provide a boundary capable of generating a reflection, since the polymer and the core of an optical fiber have refractive indexes that match. The thickness of the polymer diaphragm can be measured using a spectrometer; the output of the spectrometer is a sinusoidal curve. Two adjacent peaks can be used to calculated the Fabry-Pérot cavity length using

$$L_c = \frac{\lambda_1 \lambda_2}{2(\lambda_2 - \lambda_1)}. \quad (3.1)$$

Given the availability of the spectrometer in the lab, which has a bandwidth between 600 nm and 900 nm, the minimum detectable cavity length can be determined as 900nm. Given that the thickest diaphragm measures 970 nm prior to stress induced thinning, the equipment does not have the necessary measurement range. This was confirmed experimentally.

The previously described method may result in inaccurate readings due to further thinning of the membrane as a result of contact with the interrogation fiber. To avoid this, the interrogation fiber should not be brought in contact with the diaphragm. Instead, a small air gap should remain between the fiber endface and the diaphragm. This configuration results in two Fabry-Pérot cavities; the spectrum generated would contain a high frequency sinusoidal wave corresponding to the larger air gap between the fiber and the diaphragm, and a low frequency sinusoidal wave corresponding to the diaphragm thickness. Equation (3.1) can still be used in this configuration. No metal layer is required on the fiber endface since air induces a refractive index mismatched boundary to generate reflections.

Another method of retaining the proper physical characteristics of the diaphragm is possible. This method relies on knowing the first and second natural frequencies of the diaphragm. Given those two frequencies, the two unknowns, namely tension and diaphragm thickness, can be calculated. However, the data presented in Figure 3-8 does not clearly show a second natural frequency. A vibrometer was therefore used in an

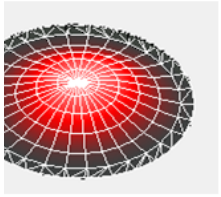

4

ıragm

attempt to obtain the first and second natural frequencies of the sensor diaphragm. The vibrometer measures the velocity magnitude spectrum of the diaphragm stimulated using a white noise acoustic signal. The vibrometer data is shown in Figure 3-10 along with the method of fixing the sensor under the vibrometer and the mode shapes at discrete, labeled frequencies. A second mode is not visible, and thus, the proposed method of obtaining the thickness and tension of the diaphragm is not possible at this point and will be conducted in future work.

Diaphragm Tension Approximation

Since none of the experimental approaches yield usable data, a numerical solution is used to approximate the diaphragm thickness and tension after application to the sensor housing. The Matlab code in Appendix A, which is based on the model by Yu *et al.* [62], is modified to calculate discrete combinations of diaphragm thickness and tension that yield a natural frequency of 5 kHz. The results are shown in Figure 3-11 and were obtained within ±0.1% of 5kHz. With zero tension, the largest thickness able to achieve

the first natural frequency of 5 kHz is 400 nm. Given the viscoelastic properties of the

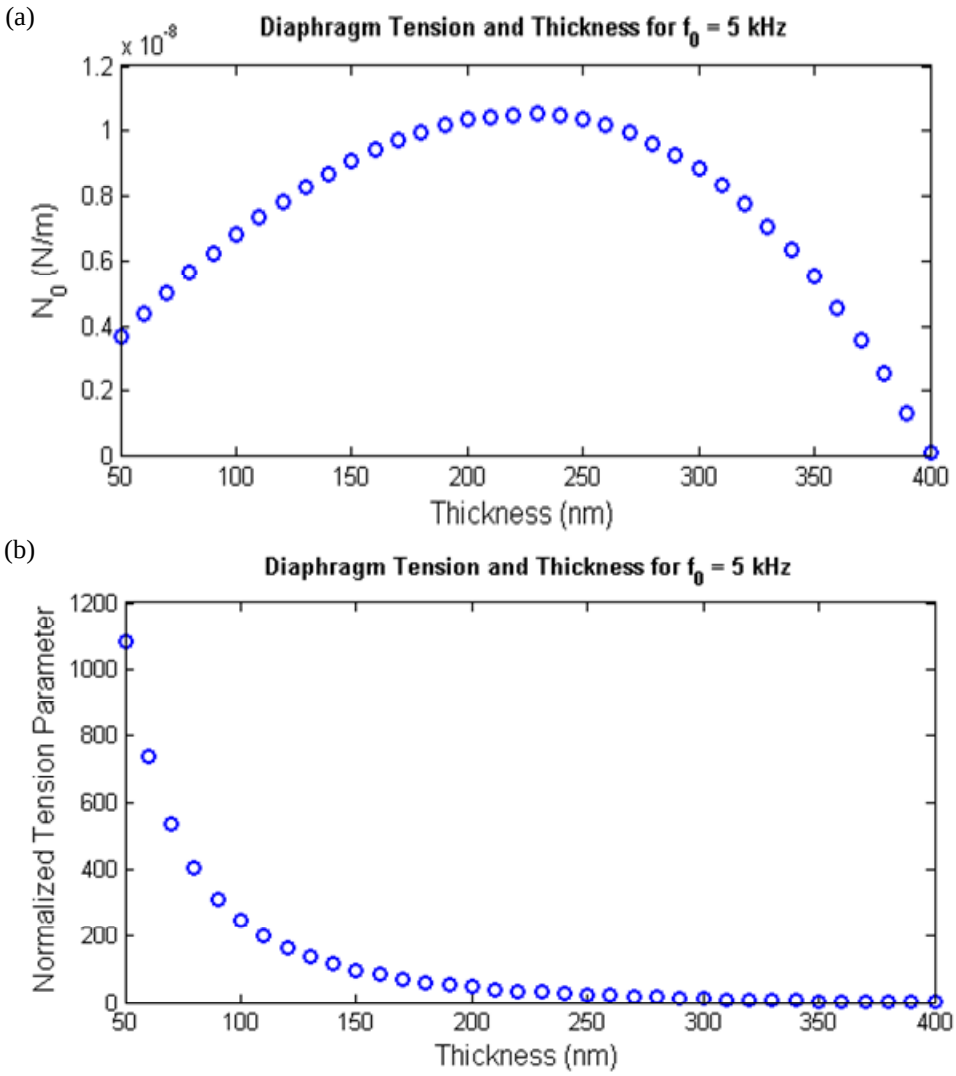

Figure 3-11. (a) Diaphragm thickness and Tension combinations resulting in a natural frequency of 5 kHz. (b) Diaphragm thickness and Normalized Tension Parameter combinations resulting in a natural frequency of 5 kHz.

diaphragm material and the large difference between the pre-application diaphragm thickness of 970 nm and the thickest possible thickness able to have a 5 kHz first natural frequency, it is reasonable to assume that all tension generated during the curing and diaphragm recession process was dissipated by reducing the thickness of the membrane. The tension parameter defined by Yu *et al.* is equivalent to the square root of the normalized tension parameter in Figure 3-11 (b), and it indicates that plate behavior

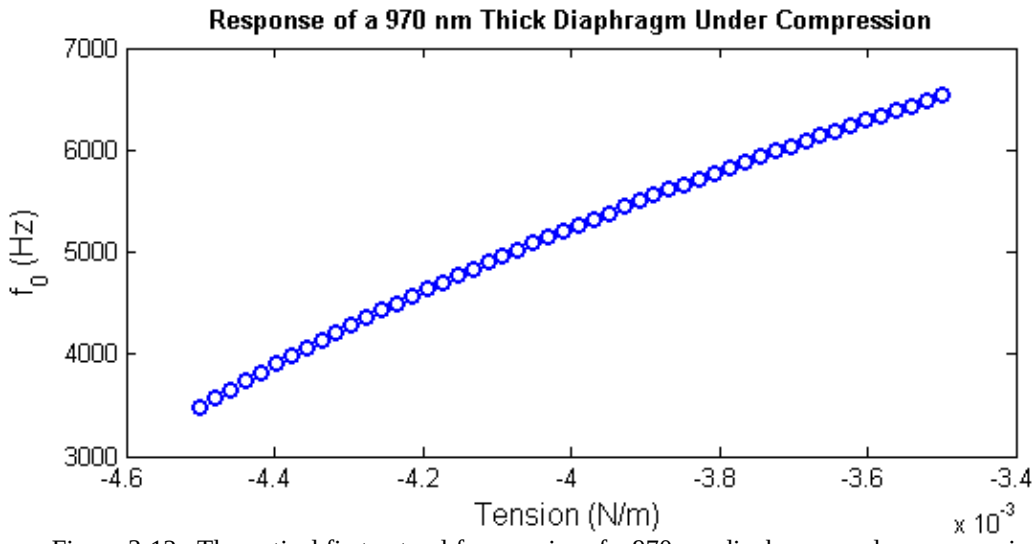

Figure 3-12. Theoretical first natural frequencies of a 970 nm diaphragm under compression.

dominates for thicknesses larger than or equal to 360 nm and membrane behavior dominates for thicknesses smaller than or equal to 80 nm. All thicknesses in between these two thresholds exhibit a transition from plate behavior to membrane behavior.

The most likely explanation for the discrepancy between the theoretical and experimental natural frequencies is supported by the diaphragm wrinkles visible in the SEM image in Figure 3-2. This type of diaphragm behavior is indicative of compression instead of tension. Only small compressive forces are necessary to significantly lower the first natural frequency of the diaphragm. As shown in Figure 3-12, the tension required to reduce the first natural frequency of the diaphragm under investigation from over 12 kHz to 5 kHz is a mere 4.1 N/m of compression. This value is reasonably small and represents the most likely explanation for the discrepancy of the first natural frequency.

3.3.2 Dynamic Range

Dynamic range is the ratio between the largest and smallest detectable signals. The human sense of hearing has an exceptionally large dynamic exceeding 100 dB

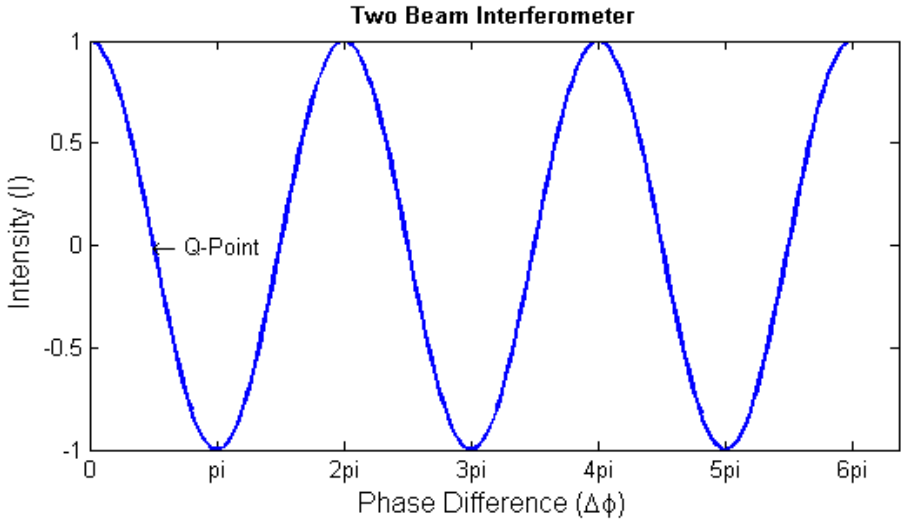

Figure 3-13. Output of a typical two beam interferometer with one of multiple quadrature points labeled.

and it is therefore desirable to develop a microphone with similar performance. The dynamic range of the sensor is determined by the optical detection system. To achieve the largest possible dynamic range for a two-beam interferometer like the system under investigation, the sensor must operate at a point at which the sensitivity is the largest, known as the quadrature point. The output of a typical two-beam interferometer is shown in Figure 3-13. The system exhibits a quasi-linear, unambiguous response if the phase difference, $\Delta\theta$, which is a function of the diaphragm deflection amplitude, A, does not exceed $\pm\frac{\pi}{2}$ with respect to the quadrature point, which defines the upper limit of the dynamic range. The phase difference is defined as

$$\Delta\phi = k_0 OPD = \frac{2\pi}{\lambda} n\Delta L = \frac{4\pi}{\lambda} A \quad , \tag{3.2}$$

and the intensity output, I, is defined as

$$I = C + D\cos\Delta\phi \quad . \tag{3.3}$$

The quadrature point can be freely chosen from the points that satisfy the condition of $\Delta\phi = (2k+1)\frac{\pi}{2}$, where k = 0,1,2,3… The lower limit is defined when the SNR = 1.

To determine the dynamic range, experiments were carried out inside an anechoic chamber to discretely increase the amplitude of a pure tone at a frequency of 1 kHz. The data shown in Figure 3-14 indicates that the upper and lower bounds of the dynamic range were not reached during the experiment since the data remains linear at the upper and lower bounds. The data is linear in the range from 45.9 dB SPL to 91.0 dB SPL, which yields a measured dynamic range of approximately 45.4 dB.

The upper limit of the dynamic range was reached in a separate experiment outside of the anechoic chamber. It is calculated to be 117.55 dB SPL, which increases

liaphragm.

the dynamic range of the sensor to 71.7 dB. Utilizing the measured noise floor of the sensor, which is discussed later in this chapter, yields an even larger dynamic range of 79.7 dB; this value is reasonably close to the desired 100 dB level. Note that the maximum phase change corresponding to the upper limit provides additional information.

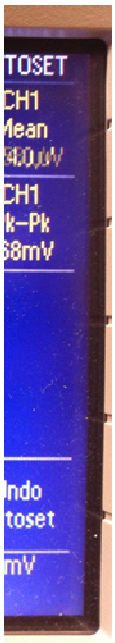

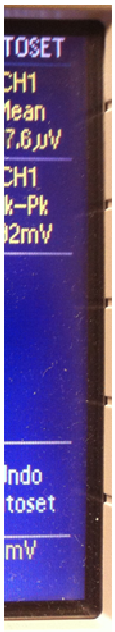

ound the quadrature

Applying the maximum allowable phase change of $\frac{\pi}{2}$ to (3.2) yields a theoretical maximum diaphragm deflection of

$$A = \frac{\lambda}{8}. \tag{3.4}$$

Given the wavelength of the light source of 1310 nm, the theoretical maximum deflection amplitude can be calculated to be 163.75 nm. The sound pressure at which this deflection is reached can be determined experimentally by observing the optical sensor response as shown in Figure 3-15, given a pure tone stimulus. Prior to leaving the linear region around the quadrature point, the response of the microphone exhibit a waveform as shown in Figure 3-15 (a), while a slight increase in sound volume beyond that point yields a waveform shown in Figure 3-15 (b).

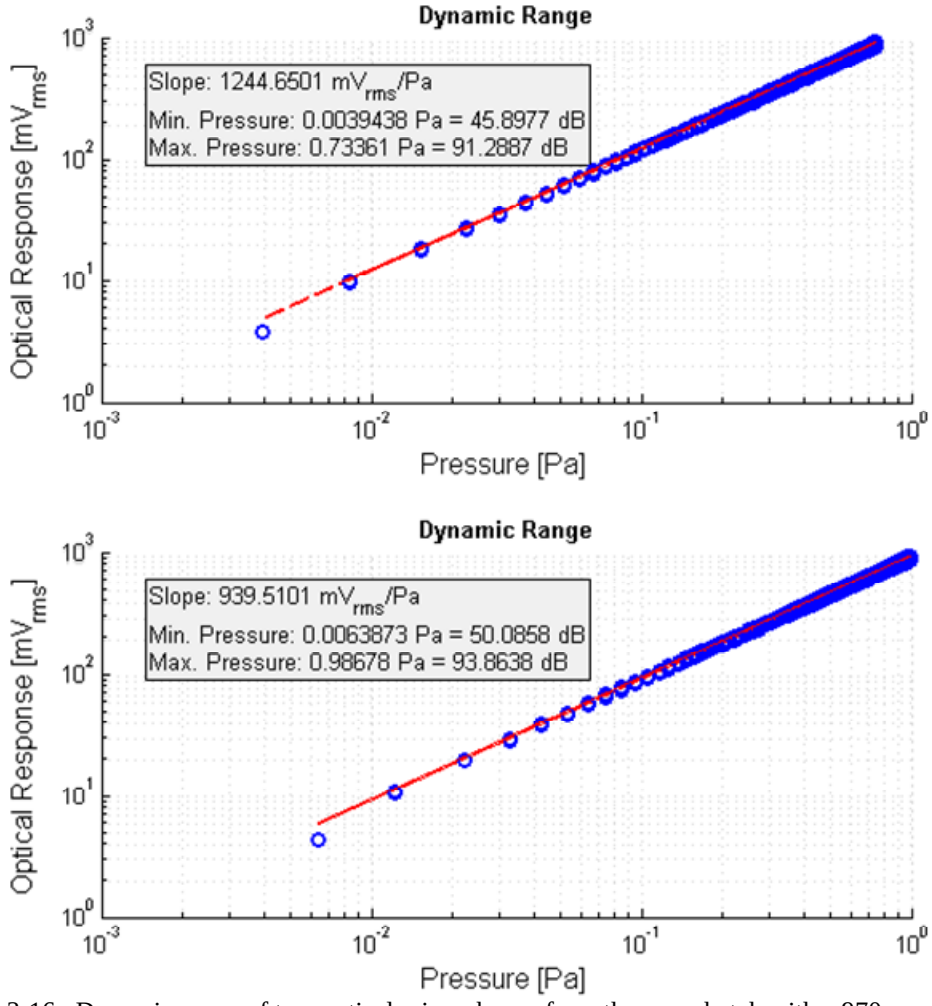

Figure 3-16. Dynamic range of two optical microphones from the same batch with a 970 nm diaphragm

3.3.3 Sensitivity

Sensitivity is the rate of change with which the sensor output changes relative to the input. The sensitivity of the microphone depends directly on the gain of the photodetector and thus can easily be adjusted to meet the requirements. The photodetector (New Focus 2011) used in the experiment has a gain setting of 24,000 V/mW, which is not an unusually high value for a photodetector.

The sensitivity of a sensor can be determined by determining the slope of a dynamic range curve, such as the one shown in Figure 3-14 or Figure 3-16. The best sensitivity measured exceeds 1 V/Pa. As discussed in Section 3.3.2, the sensitivity of a sensor depends on operating it in the vicinity of the quadrature point. A sensor can be tuned to operate at this point by matching the sensing and reference cavities, L_s and L_r, respectively, as discussed in Section 2.2.2. The quadrature point is determined experimentally by adjusting L_r until the output is a pure sinusoidal curve with maximum amplitude and symmetry across the x-axis.

Utilizing the pressure measured by the reference sensor at the point where the deflection exceeds the linear range around the quadrature point as discussed section 3.3.2, enables the sensitivity calculation in terms of diaphragm deflection. The resulting sensitivity is 10.86 nm/Pa.

3.3.4 Bandwidth

The bandwidth is the range of contiguous frequencies over which the microphone is able to accurately record sounds. The bandwidth of a human ear is 20 Hz to 20 kHz. Due to the limitation of the speaker, the experimentally achievable lower bound was limited to 50 Hz. Figure 3-17 shows the time and frequency domain responses at three

discrete frequencies. The increasing jaggedness with frequency is a result of sampling rate limited to 96 kHz by the data acquisition board. The accuracy of the data is still warranted at the largest signal frequency by the Nyquist sampling theorem. From this

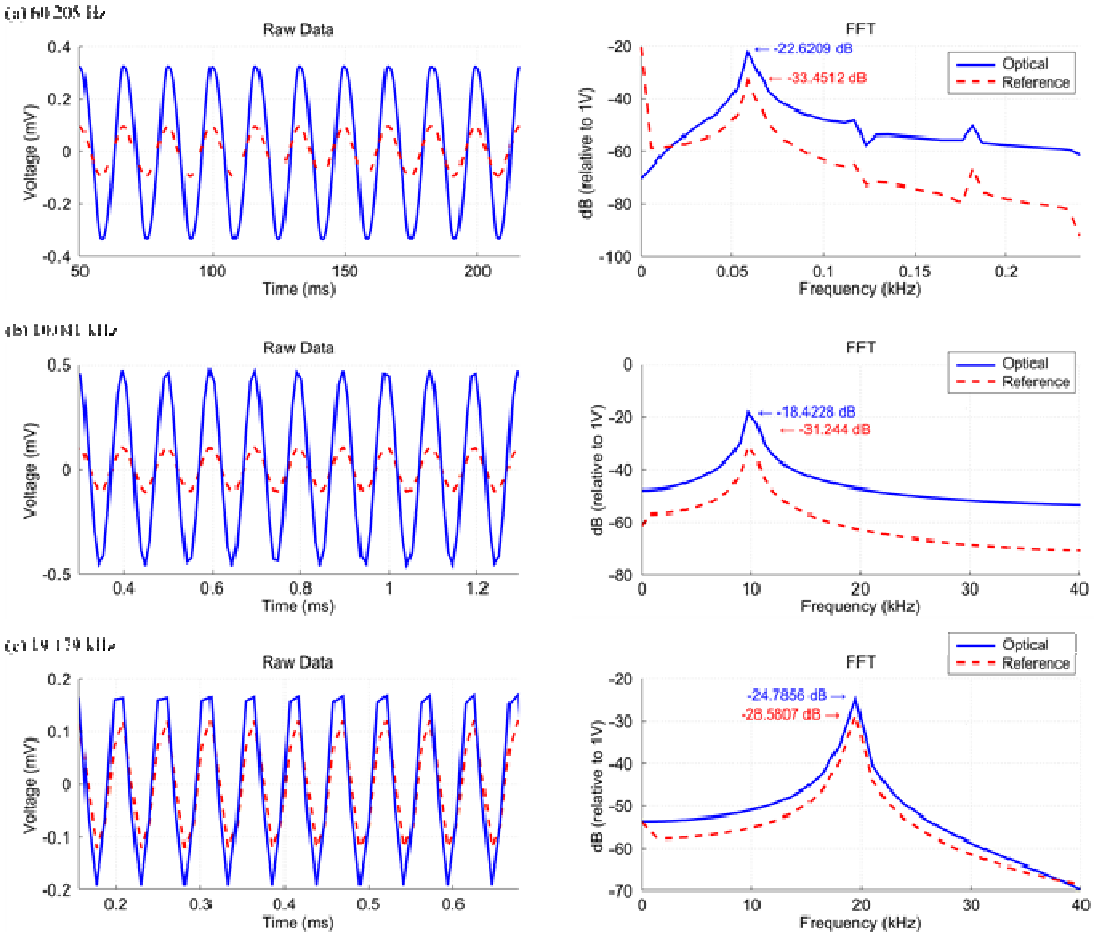

Figure 3-17. Time and frequency domain data collected at (a) 60.2 Hz, (b) 10.0 kHz, and (c) 19.2 kHz. The red line indicates data collected with the reference microphone, and the blue line indicates data collected with the optical microphone with a diaphragm thickness of 970 nm.

figure in addition to Figure 3-9, it is reasonable to conclude that the response of the sensor is very good between 50 Hz and 4 kHz and fair between 4 kHz and 20 kHz. Increasing the damping ratio of the diaphragm by tuning its pores is the most promising approach of reducing the frequency dependence of the microphone response.

3.3.5 Noise Floor

The noise floor of a system limits the smallest quantity it can detect. It is defined as the point where the SNR is equal to 1. In order to determine the noise floor of the

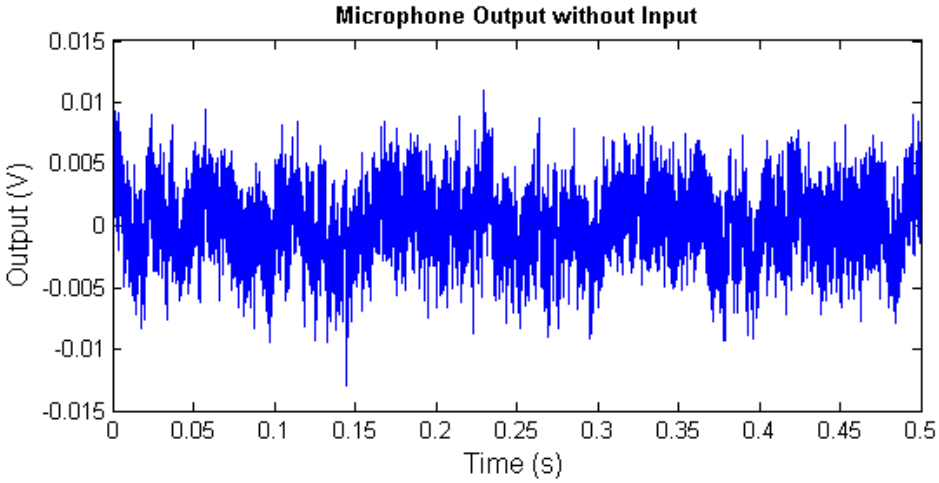

Figure 3-18. Noise floor measurement of an optical microphone inside an anechoic chamber.

microphone, the sensor is calibrated inside an anechoic chamber by sampling data without an acoustic input. The result is the noise floor as shown in Figure 3-18. Calculating the average rms noise of five trials yields a value of 1.57 mV with a standard deviation of $3.65E^{-2}$ mV. This is equivalent to 37.8 dB SPL, given the calibrated sensitivity of 1244.7 mV/Pa.

3.3.6 Signal to Noise Ratio

The signal to noise ratio is a comparison of desired signal to undesired signal. Comparing the frequency domain plots in Figure 3-17 indicates that the SNR of the reference microphone is better, but reasonably similar to that of the optical microphone.

The SNR of the optical sensor is calculated for a 94 dB reference, as it is commonly done for microphones. The calculation is simply to subtract the noise floor from 94 dB. With a noise floor of 37.8 dB, the SNR of the sensor is 56.2 dB.

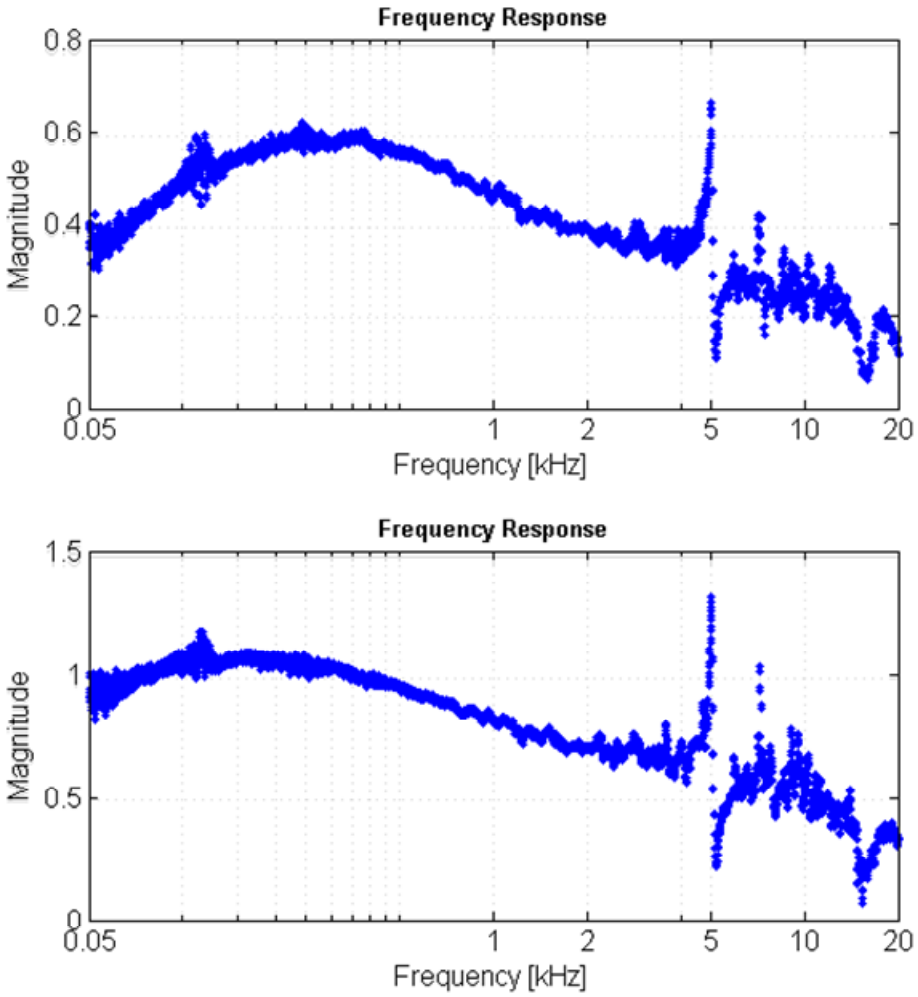

Figure 3-19. Comparison of two sensors with a 970 nm thick diaphragm fabricated from the same batch.

3.3.7 Batch Uniformity

Frequency Response

The frequency response of microphones from the same batch is very similar. The frequency response curves from two different microphones from the same batch are shown in Figure 3-19. Slight discrepancies in shape and intensity of the frequency response curves are the result of varying cleaved fiber endface quality and slight fiber misalignments. Fiber misalignment is possible because the inner diameter of the sensor housing is 25 μm larger than the diameter of an optical fiber.

Dynamic Range

The dynamic range of four sensors from the same batch of 540 nm thick diaphragm sensors was characterized to determine the batch uniformity. As shown in

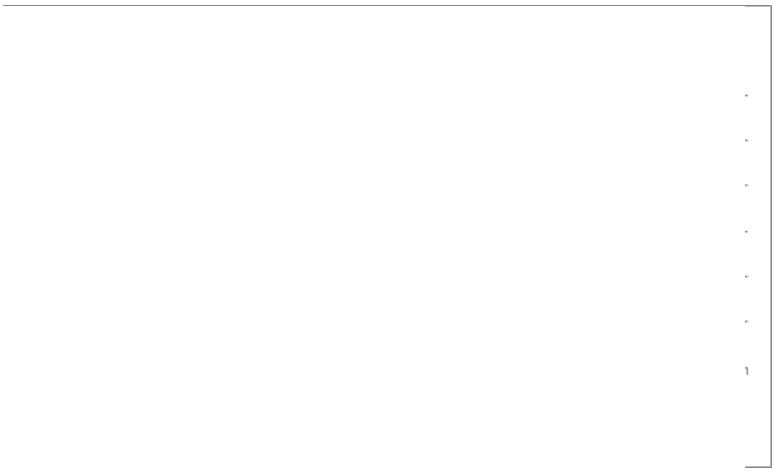

540 nm diaphragm

Figure 3-20, the dynamic range of four sensors from the same batch is uniform. Please note that the only purpose of Figure 3-20 is to demonstrate the uniformity of the batch. Due to the difference in diaphragm thickness, perfromance parameters are not comparable.

Sensitivity

The sensitivity of two microphones from the same batch is compared in Figure 3-16. While the sensitivity of both sensors is reasonable for most applications, it differs between sensors of the same batch. One reason for the discrepancy could be that inserting and fixing the fibers inside the sensor housing is an individual fabrication step at this stage of research. Since the reference cavity, L_r, only has a finite small range to adjust for differences in sensing cavity lengths, L_s, and mismatched sensing and reference cavities result in lower sensitivity since the quadrature point is not achievable, different sensitivities are expected within a batch.

Excluding the effects of the optical interrogation system, the static sensitivity, $S_{static,}$ of the sensor is given by dividing the static deflection equation, (2.1), by ΔP. The resulting equation is

$$S_{static} = \frac{3\left(1-\upsilon^2\right)a^4}{16Ed^3} \quad . \tag{3.8}$$

The sensitivity could thus be lowered by an increase in diaphragm thickness or an increase in diaphragm diameter. It is more probable that thickness variations are the cause of the discrepancy since the capillary tube diameter precision is high (±4 μm).

Bandwidth

Since the bandwidth can be deduced by examining the flat portions of the frequency response curve, Figure 3-19 indicates that bandwidth has excellent batch uniformity.

Noise Floor

A second sensor from the same batch was calibrated to have an average rms noise floor of 0.623 mV (dB SPL, Sensitivity: 939.5 mV/Pa) with a standard deviation of $5.04E^{-3}$ mV after five trials. The resulting noise floor is 30.4 dB, which matches closely with the previously calculated result.

To further improve the noise floor, the noise equivalent power of the photodetector should be improved. Noise equivalent power is the light level needed to obtain a SNR of unity.

Signal to Noise Ratio

The SNR is uniform across the batch; a second sensor with a noise floor of 30.4 dB has a SNR of 63.6 dB using the 94 dB standard, which matches the previously calibrated sensor closely.

3.4 Summary

It was determined that the sensor diaphragm is permeable to air. The permeability has been verified visually at high magnification, and experimentally by observing diaphragm deformation over time under strain caused by increased air pressure. Furthermore, it is noted that the experimental frequency response does not match the theoretical predictions. It is highly likely that the fabrication process causes a decrease in diaphragm thickness. Methods of measuring the diaphragm thickness have failed and numerical methods have not led to reasonable explanations for the discrepancy.

Furthermore, the sensor was characterized; it was found that an optical microphone exhibits a typical dynamic range from 37 to 117 dB SPL (80 dB), has an average sensitivity of 1 V/Pa, outputs an excellent frequency independent response between 50 Hz and 4 kHz and a reasonable response between 4 kHz and 20 kHz while maintaining an excellent resolution in the nano Pascal range. A performance comparison of the microphone developed in this thesis and other microphones is shown in Table 3-1. The other microphones include a commercially available Brüel & Kjær scientific

Table 3-1. Comparison of a ½" condenser microphone, an optical Fabry-Pérot microphone, a commercially available MEMS microphone, a research stage CMOS MEMS condenser microphone, and the microphone developed in this paper.

	B&K 4191 [67]	*Chitosan* [8]	*Akustica AKU340* [68]	*CMOS MEMS Condenser* [69]	*UV Polymer*
Sensitivity (mV/Pa)	12.5	2000	12.6	7.9	1245
SNR (dB)	N/A	44	62	55	58
Frequency Response (kHz)	0.0032 – 40	0.1 – 15	0.06 – 12.5	0.1 – 10	0.5 – 4.8
Dynamic Range (dB)	162	N/A	N/A	N/A	79.7
Size (mm)	12.7 Ø	0.125 Ø	2.5 x 3.35 x 1.00	2.35 x 1.65 x 1.2	0.36 Ø

microphone, an optical microphone, a commercially available MEMS microphone, and a research-stage MEMS microphone.

The sensors exhibit excellent batch uniformity due to the fabrication and assembly process of the diaphragm. Sensitivity is the only parameter that is not uniform within the batch because fiber insertion is an individual process at the current research stage with the potential for easy and inexpensive expansion to batch fabrication.

4 Sound Localization in Two Dimensions with a Linear Array

4.1 Introduction

The purpose of directional sound localization is to quickly and accurately locate the direction of the acoustic disturbance. The most common way to achieve sound localization is by using a directional microphone or a microphone array [50]. Potential applications of the technology include hearing aids, autonomous robot navigation, search and rescue vehicles, targeting systems, and gunshot localization [63]. Any of these applications would profit from sensor miniaturization; the reduced size makes the device less cumbersome to the user, more portable, and lighter. The size reduction also provides immunity from the limitations of operating in the near field that large-scale devices suffer from; near field operation negates the plane wave assumption that is commonly applied to large-scale designs. The near field assumption may no longer be applied since the effects of the wave-front curvature in the new affect the array's ability to determine the sound direction. Shrinking the array reduces the device size relative to the wave-front and thus overcomes the limitation [49]. The benefits discussed make reducing the size of a microphone array highly desirable.

Reducing the size of a microphone array is desirable, yet shrinking its dimensions too much results in a very small time difference of arrival (TDOA). TDOA refers to the time delay of wave-front arrival between a distinct pair of microphones in the array. Several groups have worked on this problem, however all groups require access to expensive MEMS technology to achieve their designs [53,56,57,64,65]. The work presented here will utilize linear arrays of multiple micro-scale microphones to

approximate the direction of the sound source relative to the array. While the size of these arrays is larger than their MEMS counterparts, their cost and ease of fabrication is preferable, making them ideal devices for disposable applications.

4.2 Analytical Sensor Array Evaluation

The goal of initial simulations is designed to determine if a linear array of microphones is capable of localizing a sound source in a 2 dimensional (2D) plane. The localization method is triangulation, which is one of the simplest and least computationally expensive localization algorithms that can easily be applied to a large array.

4.2.1 Localization Algorithm

For 2D sound localization utilizing triangulation, an array of at least 3 microphones is required. A 3-microphone array provides 3 distinct pairs of microphones that generate TDOA data. The TDOA data for each pair yields an angle approximation which can be used to generate the equation of a vector given the spacing between the microphones in the array. The intersection of the 3 directional vectors should give a reasonable approximation of the sound source location in a 2D plane.

For simulation purposes, the microphone array is assumed to be located along the x-axis with microphones facing towards the positive y direction. The origin of the array is in the geometric center of the array, and the sensors are spaced equidistant, such that adjacent sensors are separated by a known distance, d. For the simulation, the sound source location is known; the location is specified by the distance, r, from the origin of the array to the sound source and the angle, θ, also measured from the origin of the array

as shown in Figure 4-1. Given the distance, *r*, the angle, *θ*, and the uniform microphone

separation distance, *d*, all other microphone pair angles can be calculated. For the 3-microphone example shown in Figure 4-1, the other two angles are equal to

$$\theta_{12} = \tan^{-1}\left(\frac{r\sin\theta_{13}}{r\cos\theta_{13} - \frac{\delta_{13}}{2}}\right) = \tan^{-1}\left(\frac{\sin\theta_{13}}{\cos\theta_{13} - \frac{\delta_{13}}{2}}\right) \tag{4.1}$$

and

$$\theta_{23} = \tan^{-1}\left(\frac{\sin\theta_{13}}{\cos\theta_{13} + \frac{\delta_{13}}{2}}\right), \tag{4.2}$$

where

$$\delta_{ij} = \frac{d_{ij}}{r} . \tag{4.3}$$

Using geometry and the angles θ_{13} and θ_{23}, the intersection of the two vectors can be calculated using

$$x_1 = \frac{\frac{d}{2}\tan\theta_{23}}{\tan\theta_{13} - \tan\theta_{23}} \tag{4.4}$$

and

$$y_1 = \frac{\frac{d}{2}\tan\theta_{23}\tan\theta_{13}}{\tan\theta_{13} - \tan\theta_{23}} . \tag{4.5}$$

The remaining two intersections can be calculated similarly using the angles θ_{13}, θ_{12} and θ_{23}, θ_{12}, respectively, as the following

$$x_2 = \frac{d}{2} + \frac{\frac{d}{2}\tan\theta_{13}}{\tan\theta_{12} - \tan\theta_{13}} , \tag{4.6}$$

$$y_2 = \frac{\frac{d}{2}\tan\theta_{23}\tan\theta_{13}}{\tan_{13} - \tan\theta_{23}} , \tag{4.7}$$

and

$$x_3 = \frac{d}{2} + \frac{d\tan\theta_{23}}{\tan\theta_{12} - \tan\theta_{23}} , \tag{4.8}$$

$$y_3 = \frac{d\tan\theta_{23}\tan\theta_{12}}{\tan_{12} - \tan\theta_{23}} . \tag{4.9}$$

Sensitivity Analysis

These equations can be expanded to simulate the localization abilities of a linear equally spaced array composed of any given number of microphones. Table 4-1 shows

several important parameters for linear microphone arrays containing 3 to 10 microphones. As the number of microphones increases, there are a certain number of microphone pairs that will produce the same angle θ as other pairs; these angles are classified as overlaps and result in a significant reduction of pairs used for the calculation of the sound source location. With the simplification, only the primary θs need to be calculated. Since current sound localization arrays have directional localization errors of ±3°, the purpose of the simulation is to determine if this type of array is capable of localizing a sound source in 2D and how many microphones it requires to locate a sound source successfully given different degrees of random error in the angles, θ, calculated by each microphone pair. The Matlab code can be found in Appendix C. NO NUMERICAL SIMULATION RESULTS.

Table 4-1. Parameters for microphone arrays with 3 to 10 microphones.

# of Mics	n	# of θs	# of Pairs	Overlap	Pairs Used
3	1	3	3	0	3
4	2	6	15	1	10
5	3	10	45	3	21
6	4	15	105	6	36
7	5	21	210	10	55
8	6	28	378	15	78
9	7	36	630	21	105
10	8	45	990	28	136
Formula	#Mics - 2	#Mics choose 2	#θs choose 2	$\frac{(n-1)(n)}{2}$	$2n^2+n$

# of Mics	n	Duplicate	Primary θs	Secondary θs
3	1	0	3	0
4	2	5	5	1
5	4	24	7	3
6	5	69	9	5
7	6	155	11	7
8	7	300	13	9
9	8	528	15	11
10	9	854	17	13
Formula	#Mics - 2	# Pairs – Pairs Used	#θs - Overlap	-

4.2.2 Effects of Sensor Variance on Localization Performance

Given a setup shown in Figure 4-2, where the microphone separation is given by 2*d* and *d* is defined as

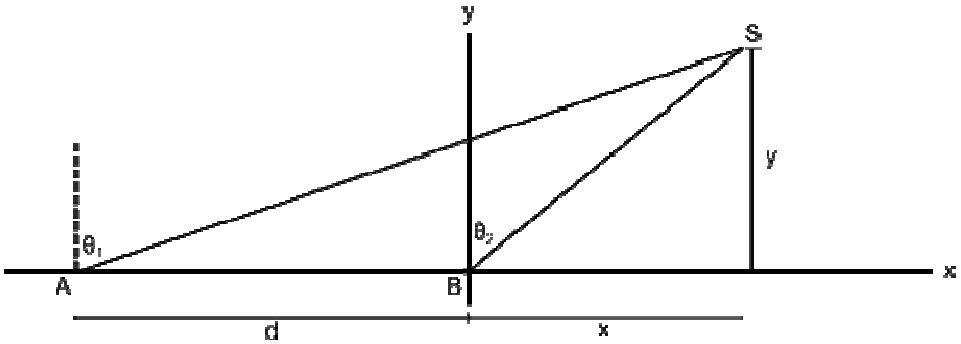

Figure 4-2. Simplified schematic of microphone array. A and B are center points in the middle of respective microphone pairs.

$$d = y\left(\tan\theta_1 - \tan\theta_2\right), \tag{4.10}$$

and the y- and x-position of the sound source by

$$y = \frac{d}{\tan\theta_1 - \tan\theta_2}, \tag{4.11}$$

$$x = y\tan\theta_2 = \frac{d\tan\theta_2}{\tan\theta_1 - \tan\theta_2}. \tag{4.12}$$

The change in *y* with respect to θ_1 and θ_2 becomes

$$\frac{\partial y}{\partial\theta_1} = -\frac{d\left(1+\tan^2\theta_1\right)}{\left(\tan\theta_1 - \tan\theta_2\right)^2} \tag{4.13}$$

$$\frac{\partial y}{\partial\theta_2} = \frac{d\left(1+\tan^2\theta_2\right)}{\left(\tan\theta_1 - \tan\theta_2\right)^2} \tag{4.14}$$

and similarly the change in *x* with respect to θ_1 and θ_2 becomes

$$\frac{\partial x}{\partial \theta_1} = -\frac{d \tan\theta_2 \left(1+\tan^2\theta_1\right)}{\left(\tan\theta_1 - \tan\theta_2\right)^2} \tag{4.15}$$

$$\frac{\partial x}{\partial \theta_2} = \frac{d \tan\theta_1 \left(1+\tan^2\theta_2\right)}{\left(\tan\theta_1 - \tan\theta_2\right)^2} \tag{4.16}$$

.

The total change of x and y then can be expressed as

$$\Delta x = \frac{\partial x}{\partial \theta_1}\Delta\theta_1 + \frac{\partial x}{\partial \theta_2}\Delta\theta_2 \tag{4.17}$$

,

$$\Delta y = \frac{\partial y}{\partial \theta_1}\Delta\theta_1 + \frac{\partial y}{\partial \theta_2}\Delta\theta_2 \tag{4.18}$$

,

and the distance squared from the origin to the sound source is equal to

$$R^2 = x^2 + y^2 = \frac{d^2\left(1+\tan^2\theta_2\right)}{\left(\tan\theta_1 - \tan\theta_2\right)^2} = f\left(\theta_1, \theta_2\right) \tag{4.19}$$

.

Differentiating both sides yields

$$2R\Delta R = \frac{\partial f}{\partial \theta_1}\Delta\theta_1 + \frac{\partial f}{\partial \theta_2}\Delta\theta_2 \tag{4.20}$$

,

which simplifies to

$$\Delta R = \frac{1}{2R}\left(\frac{\partial f}{\partial \theta_1}\Delta\theta_1 + \frac{\partial f}{\partial \theta_2}\Delta\theta_2\right) \tag{4.21}$$

.

Differentiating (4.19) with respect to θ_1 and θ_2 yields

$$\frac{\partial f}{\partial \theta_1} = -\frac{2d^2\left(1+\tan^2\theta_1\right)\left(1+\tan^2\theta_2\right)}{\left(\tan\theta_1 - \tan\theta_2\right)^3} \tag{4.22}$$

,

$$\frac{\partial f}{\partial \theta_2} = -\frac{2d^2\left(1+\tan\theta_1\tan\theta_2\right)\left(1+\tan^2\theta_2\right)}{\left(\tan\theta_1 - \tan\theta_2\right)^3} \tag{4.23}$$

.

The distance, *R*, from (4.19) can be expressed as

$$R = \frac{d\sqrt{1+\tan^2\theta_2}}{\left|\tan\theta_1 - \tan\theta_2\right|}. \tag{4.24}$$

Substituting (4.22), (4.23), and (4.24) into (4.21) can be expressed as

$$\begin{aligned}\Delta R &= \left\langle \begin{array}{l} \dfrac{\left|\tan\theta_1 - \tan\theta_2\right|}{2d\sqrt{1+\tan^2\theta_2}} \cdot \dfrac{2d^2\left(1+\tan^2\theta_2\right)}{\left(\tan\theta_1 - \tan\theta_2\right)^3} \cdot \\ \left\{-\left(1+\tan^2\theta_1\right)\Delta\theta_1 + \left(1+\tan\theta_1\tan\theta_2\right)\Delta\theta_2\right\} \end{array} \right\rangle \\ &= \frac{d\sqrt{\tan^2\theta_2}}{\left(\tan\theta_1 - \tan\theta_2\right)^2 \cdot sign\left(\theta_1 - \theta_2\right)} \left\{-\left(1+\tan^2\theta_1\right)\Delta\theta_1 + \left(1+\tan\theta_1\tan\theta_2\right)\Delta\theta_2\right\}, \\ &= \lambda_1\Delta\theta_1 + \lambda_2\Delta\theta_2 \end{aligned} \tag{4.25}$$

using the definition of variance

$$\mathrm{var}\left(R\right) = \lambda_1^2 \cdot \mathrm{var}\left(\Delta\theta_1\right) + \lambda_2^2\,\mathrm{var}\left(\Delta\theta_2\right). \tag{4.26}$$

Assuming that

$$\mathrm{var}\left(\Delta\theta_1\right) = \mathrm{var}\left(\Delta\theta_2\right) = \sigma^2, \tag{4.27}$$

(4.26) can be expressed as

$$\begin{aligned}&\mathrm{var}\left(R\right) = \sigma^2\left(\lambda_1^2 + \lambda_2^2\right) \\ &= \sigma^2 \frac{d^2\left(1+\tan^2\theta_2\right)}{\left(\tan\theta_1 - \tan\theta_2\right)^4}\left\{\left(1+\tan^2\theta_1\right)^2 + \left(1+\tan\theta_1\tan\theta_2\right)^2\right\}. \end{aligned} \tag{4.28}$$

Picking $\sigma^2 = 1$ for convenience leaves three unknowns in (4.28). Picking a constant to replace the microphone separation radius, *d*, yields Figure 4-3. The solution appears reasonable given that no solution exists if the angles θ_1 and θ_2 are parallel. The minimum points marked occur at (10, -80), and (-10, 80), indicating that the optimal region for sound localization does not occur along the y-axis, but slightly off-center. Increasing the microphone separation radius parameter, *d*, effectively increases the var(R) value of each point in Figure 4-3. Three arbitrary points on the surface of Figure 4-3

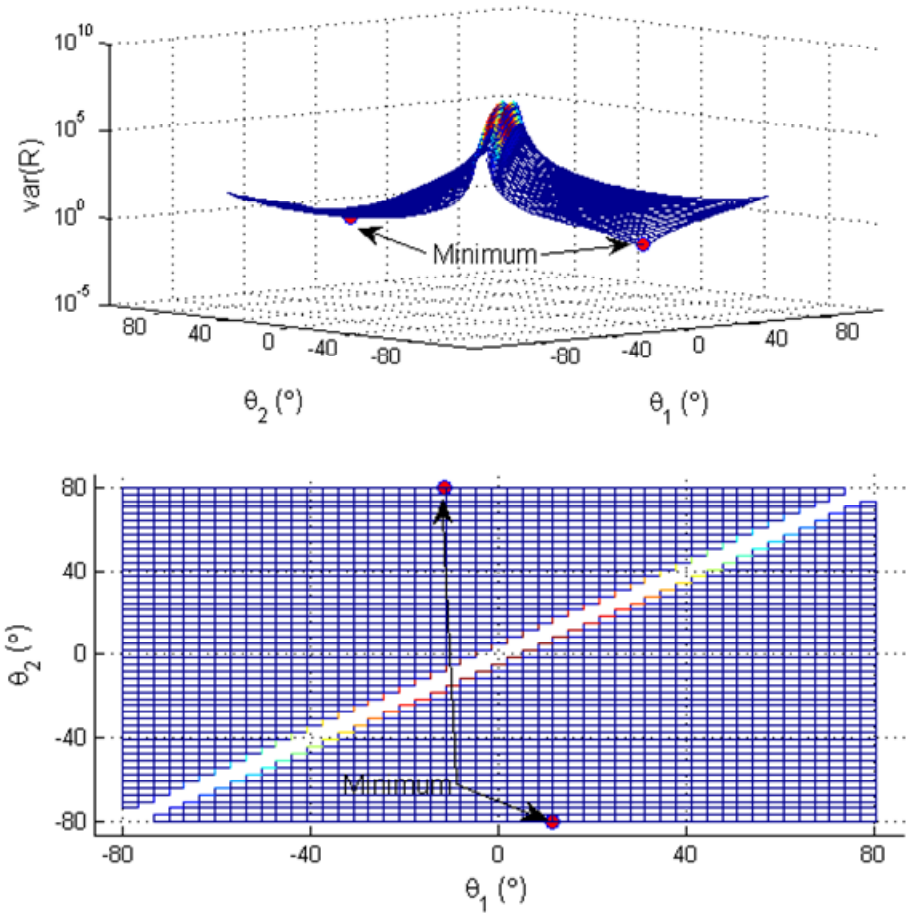

Figure 4-3. Analytical solution of sensor variance assuming a constant microphone separation, d.

were investigated for several values of *d* as shown in Figure 4-4. The variance increases exponentially with larger microphone spacing for all combinations of θ_1 and θ_2. The rate

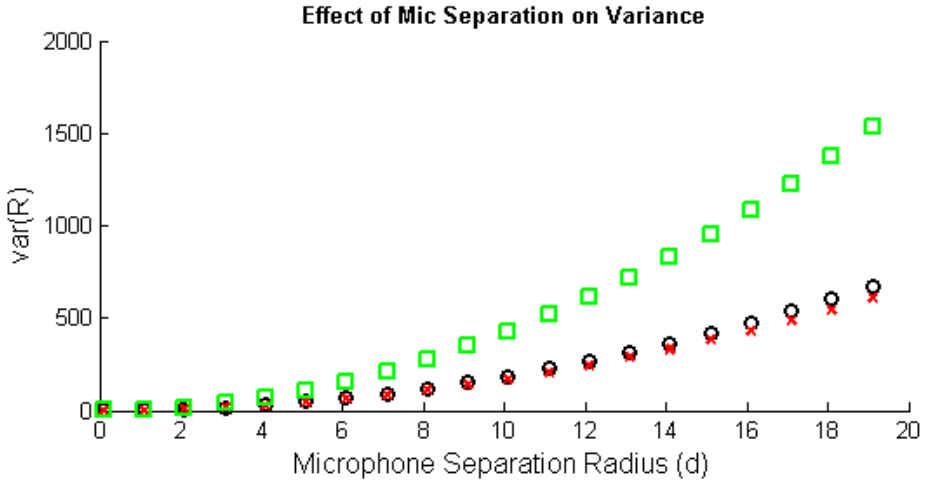

Figure 4-4. Effect of Microphone Separation on Sensor Variance

of increase for var(R) with respect to *d* is the strongest for points located near the asymptote.

4.3 Experimental Results

A 3-microphone array was fabricated and set up as shown in Figure 4-5. To ensure precise angle control, the sound source was fixed and the array itself was rotated

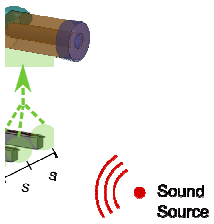

using a motorized rotational stage. Stage rotation was defined as shown in Figure 4-6. The array was rotated from -80° to 80° using a 10° interval and each location was interrogated 5 discrete times at a sampling rate of 96 kHz. A puretone 1 kHz signal was selected as the sound source to reduce the separation distance between sound source and array. A 1 kHz acoustic signal has a wavelength of 34.029 cm, which, assuming a distance of 10λ to ensure plane wave propagation, results in 3.4029 m array to sound source separation distance. To ensure plane wave behavior, the separation distance was increased to 4 m for the experiment. Several microphone separation distances were experimentally tested with the best results obtained at a distance of 3 cm.

The direction of the sound source is located using the interaural phase difference (IPD) for each combination of the three microphones in the array. The theoretical

4-8. Determining
ıral time difference
1-3, and 2-3).se

maximum IPD occurs when the array is rotated to a θ = ±90° and can be expressed by

$$IPD_{\max} = \left(\frac{s * f_a}{c} \right) 360^{\circ}, \tag{4.29}$$

where IPD_{max} represents the maximum interaural phase difference, s represents the microphone separation, f_a represents the sound frequency, and c represents the speed of sound. The agreement between theoretical and experimental data shown in Figure 4-7 is excellent, indicating that the direction of a sound source can be obtained with high accuracy. At each angle, θ, 5 measurements were taken, but data points are for the most part indistinguishable in Figure 4-7, indicating that the sensors are very precise.

The 2D sound localization algorithm discussed at the beginning of this chapter did not produce presentable data.

4.4 Summary

It has been demonstrated that a simple array of three miniature fiber optic microphones with a separation distance of 3 cm is capable of accurately and precisely locating the direction of a sound source.

5 Summary and Future Work

5.1 Summary and Thesis Contributions

An ultraminiature polymer-based fiber optic microphone and a miniature array have been developed in this thesis work. The sensor was designed to feature a low-finess Fabry-Pérot cavity structure formed by a fiber end facet and a nanometer-scale polymer diaphragm covering a ferrule-supported cavity. The overall diameter is approximately equivalent to three optical fibers side by side (360 μm). In addition to the advantages offered by most fiber optic sensors including light weight, high sensitivity, immunity to EMI, and remote sensing capabilities, there are several novel aspects of the sensor. First, the unique sensor fabrication technique employs simple, inexpensive processes and safe procedures, and it also allows for batch sensor production that yields good device-to-device uniformity. Second, the diaphragm thickness and cavity length of the microphones can be easily tailored to fulfill the requirements of different sensitivity, bandwidth, and measurement range for various applications. Third, the sensor interrogation subsystem has a high degree of immunity to environment perturbations, and yields high sensitivity (even for miniature-sized microphones), high speed, high resolution, and low noise.

Multiple sensors with different diaphragm thicknesses were fabricated and calibrated. Batch uniformity was found to be very good for all performance parameters other than sensitivity. Sensitivity strongly depends on the cavity length of the sensor matching that of the reference cavity. Cavity length adjustment was done individually for all sensors. Discrepancies in sensitivity were therefore expected.

After calibration, experimental studies were used to show that an array of sensors is capable of carrying out sound source localization in two dimensions.

The original contributions of this thesis work can be summarized as the following:

- This is the first time an ultraminiature fiber optic microphone is developed by using UV batch fabrication technique.
- For the first time, polymer based micro-scale acoustic sensors were used in a sound localization array capable of localizing a sound source in two dimensions.

5.2 Future Work

Although this research entailed the design, modeling, analysis, fabrication, and experimental study of a micro-scale polymer based sensor, there is still further research to be carried out, before this sensor can be considered to be complete.

Further miniaturization of the sensor is possible. A proof of concept sensor with a 100 μm diaphragm microphone based on the same design and fabrication techniques is shown in Appendix D. Further miniaturization would require switching from a ferrule based sensor structure to a UV molded or fiber-etched structure.

Increasing the tension of a very thing diaphragm is critical to achieve high sensitivity while maintaining large bandwidth. Further research into materials and fabrication techniques would likely produce a significant increase in sensor performance. Developing chemical or mechanical patterning processes to control the size and distribution of pores on the diaphragm with the goal of precisely controlling and increasing the damping ration of the diaphragm could also lead to desirable results.

Determining a specific application and tailoring the performance and packaging of the sensor to meet the requirements of that application is the final step. If sound localization applications are further pursued, two and three dimensional localization arrays can be further investigated.

Appendix A

```
% Assume constant damping factors
clear; close all; clc;

rho = 1.1e3;
% density, kg/m^3
E = 20.7e6;
% young's modulus, pa
nu = 0.4;
% poisson's ratio
h = 0.54e-6;
% thickness, m
a = 75e-6;
% radius, m
N0 = 0;
% tension, N/m^2
D = E*h^3/12/(1-nu^2);
% flexural stiffness
s = pi*a^2;
% surface area
mp = rho*s*h;
% mass, kg
chi_td = N0*a^2/D;
% normalized tension parameters
kp = pi*D/a^2;
% stiffness parameter
xi_arr = [0.01 0.1 0.25 0.5];
% damping factors
p_ref = 20e-6;
SPL = 100;
spa = p_ref*10^(SPL/20)*sqrt(2);
NMD = 10;
freq_arr = linspace(0,40,401);
omega_arr = 2*pi*freq_arr*1e3;
omega_arr = omega_arr(:);
[ALPHA,Ud] = getPlateModes(chi_td,NMD);
lambda_p = sqrt(kp/mp);
omega_mn = lambda_p*ALPHA;
disp(['First resonant frequency: ' num2str(omega_mn(1)/2/pi) 'Hz'])

for ij = 1:length(xi_arr)
    xip = xi_arr(ij);
    mag(ij,:) = getResp(omega_arr,chi_td,spa,NMD,s,kp,mp,xip);
end
amp = abs(mag)*1e9;
sensitivity = abs(mag)/spa;

hf1 = figure('Position',[100 300 400 300]);
plot(freq_arr,amp(1,:),'b-','LineWidth',2)
hold on
plot(freq_arr,amp(2,:),'r-.','LineWidth',2)
plot(freq_arr,amp(3,:),'g--','LineWidth',2)
plot(freq_arr,amp(4,:),'m:','LineWidth',2)
xlim([0 30])
hlg = legend(['$\xi = ' num2str(xi_arr(1)) '$'],...
```

```
    ['$\xi = ' num2str(xi_arr(2)) '$'],...
    ['$\xi = ' num2str(xi_arr(3)) '$'],...
    ['$\xi = ' num2str(xi_arr(4)) '$'],'Location','Best');
set(hlg,'interpreter','latex')
set(gca,'YScale','log')
xlabel('Sound frequency (kHz)','interpreter','latex')
ylabel(['Amptitude for ' num2str(SPL) 'dB SPL (nm)'],...
    'interpreter','latex')

hf2 = figure('Position',[600 300 400 300]);
plot(freq_arr,sensitivity(1,:),'b-','LineWidth',2)
hold on
plot(freq_arr,sensitivity(2,:),'r-.','LineWidth',2)
plot(freq_arr,sensitivity(3,:),'g--','LineWidth',2)
plot(freq_arr,sensitivity(4,:),'m:','LineWidth',2)
xlim([0 30])
hlg = legend(['$\xi = ' num2str(xi_arr(1)) '$'],...
    ['$\xi = ' num2str(xi_arr(2)) '$'],...
    ['$\xi = ' num2str(xi_arr(3)) '$'],...
    ['$\xi = ' num2str(xi_arr(4)) '$'],'Location','Best');
set(hlg,'interpreter','latex')
set(gca,'YScale','log')
xlabel('Sound frequency (kHz)','interpreter','latex')
ylabel('Sensitivity (m/Pa)','interpreter','latex')


%getResp: calculate the response of two diaphragms when excited at
certain
%   frequency and incident angle
%
%   Usage: [mag1,mag2,phi1,phi2] = getResp(Hd,Ud,chi_lambda,SPA,angle)
%
%   INPUT:
%       omega       -   sound frequency, rad/s
%       chi_td      -   tension parameter
%       spa         -   sound pressure amplitude
%       NMD         -   number of used modes
%       s           -   membrane area, s = pi a^2
%       kp          -   membrane stiffness, kp = pi D/a^2
%       mp          -   membrane mass, mp = rho s h
%       xi          -   damping factors for all modes
%
%   OUTPUT:
%       mag         -   Deflection amplitude of membrane

function mag = getResp(omega,chi_td,spa,NMD,s,kp,mp,xip)

PHI0 = 1/sqrt(2*pi);
[ALPHA,Ud] = getPlateModes(chi_td,NMD);
lambda_p = sqrt(kp/mp);
omega_mn = lambda_p*ALPHA;
syms r;
Fpmn = zeros(NMD,1);
Wpmn = zeros(length(omega),NMD);
mag = zeros(length(omega),1);
for mn = 1:NMD
```

```
    integral = spa*Ud(mn)*r;
    Fpmn(mn) = quad(vectorize(inline(char(integral),'r')),0,1);
    Fpmn(mn) = Fpmn(mn,1)*2*pi*PHI0;
    den = 1-(omega/omega_mn(mn)).^2+j*2*xip*omega/omega_mn(mn);
    Wpmn(:,mn) = Fpmn(mn)*s/kp/ALPHA(mn)^2./den;
    mag = mag+Wpmn(:,mn)*double(subs(Ud(mn),r,0))*PHI0;
end
end


%getPlateModes: find axisymmetric mode shapes and natural frequencies
of
%   a cicular plate with initial tension
%
%   Usage: [ALPHA,Ud] = getPlateModes(chi_td,NMd)
%
%   INPUT:
%           chi_td      -   Normalized tension parameter
%           NMd         -   Number of modes to extract
%
%   OUTPUT:
%           ALPHA      -   Normalized natural frequencies
%           Ud          -   Mode shape functions

function [ALPHA,Ud] = getPlateModes(chi_td,NMd)

PHI0 = 1/sqrt(2*pi);                %   Plate' 0th mode in circum. dir.
zero_tol = 1e-8;
intg_tol = 1e-8;
options = optimset('TolX',zero_tol);
syms r alpha2;
alpha1 = sqrt(alpha2^2+chi_td);

%   Mode shape function

funUd = besselj(0,alpha2*r)-besselj(0,alpha2)/...
    besseli(0,alpha1)*besseli(0,alpha1*r);
dfunUd = diff(funUd,'r');

%   Apply clamped boundary condition at r=1

zero_d = vpa(subs(dfunUd,r,1));

%   Find the roots

alpha2_step = 0.05;
if (chi_td < 0)
    alpha2_value1 = sqrt(-chi_td);
else
    alpha2_value1 = 0;
end
alpha2_value2 = alpha2_value1+alpha2_step;
n = 1;
while (n <= NMd)
```

```
    if
(subs(zero_d,alpha2,alpha2_value1)*subs(zero_d,alpha2,alpha2_value2) <
0)
        ALPHA2(n) = fzero(inline(char(zero_d)),...
            [alpha2_value1,alpha2_value2],options);
        ALPHA1(n) = sqrt(ALPHA2(n)^2+chi_td);
        Ud(n) = besselj(0,ALPHA2(n)*r)-besselj(0,ALPHA2(n))/...
            besseli(0,ALPHA1(n))*besseli(0,ALPHA1(n)*r);
        ALPHA(n) = ALPHA1(n)*ALPHA2(n);

%   Normalize mode shape function

        integral = vpa(Ud(n)*Ud(n)*r);
%         Cpmn =
quad(vectorize(inline(char(integral),'r')),0,1,intg_tol);
        Cpmn = simplify(int(integral,r,0,1));
        Cpmn = abs(Cpmn);
        Ud(n) = vpa(Ud(n)/sqrt(Cpmn));

        n = n+1;
    end
    alpha2_value1 = alpha2_value2;
    alpha2_value2 = alpha2_value1+alpha2_step;
end
```

Appendix B

```
FINISH
/CLEAR,NOSTART
/TITLE, SINGLE-layer circular membrane

TH = 0.54E-6                    ! thickness of the mid layer, m
RADIUS = 75e-6                  ! radius, m
EMID = 20.7E6                   ! Young's modulus of the mid layer, Pa
NUMID = 0.4                     ! Poisson's ratio of the mid layer, Pa
RHO = 1100                      ! DENSITY

PRES_PSI = 1                    ! Applied pressure level in psi
PRES_PA = PRES_PSI*6.8927e3

/PREP7

! Define material properties
MP,EX,1,EMID
MP,PRXY,1,NUMID
MP,DENS,1,RHO

! Select element type and real constant
ET,1,SHELL99
R,1,1
RMORE
RMORE,1,0,TH

! Create the geometry
CYL4,0,0,RADIUS             !Change value of RADIUS to vary membrane diameter
HPTCREATE,AREA,1,100,COORD,0,0,,0

! Mesh
LESIZE,ALL, , ,41, , , , ,1
AMESH,ALL

! Boundary conditions
CSYS,1
NSEL,S,LOC,X,RADIUS
CM,NBOUND,NODE
D,ALL, , , , , ,ALL, , , , ,
NSEL,ALL

NSEL,S,LOC,X,0
CM,NCENTER,NODE
ALLSEL,ALL
CSYS,0
```

```
FINISH

/SOLU
ANTYPE,2
MODOPT,LANB,20
EQSLV,SPAR
MXPAND,20, , ,0
MODOPT,LANB,20,0,100E3, ,OFF
SOLVE
FINISH

/POST1
SET,LIST
FINISH
```

Appendix C

```
clear; close all; clc
%% Parameters
DE = [0,.1,.2];
%Directional Error [deg]
A = [10,40,90].*(pi/180);
% Angle [rad]
MS = [0.1,5,10];
% Microphone Separation [cm]
D = [5,500,1000];
% Sound Source to Array Distance [cm]
times = 1000;
% Number of iterations
sigma = 2;
% 2sigma = 68.2%, 4sigma = 95.4%, 6sigma = 99.9%\
M = 3;
% Number of microphones
N = M-2;
T1 = 3+2*(N-1);
% First row thetas
U = 2*N^2+N;
% Number of usable theta pairs
Ts = size(combntns(1:M,2),1);
% Number of thetas
Ps = size(combntns(1:Ts,2),1);
% Number of pairs
Du = Ps-U;
% Duplicates to be ignored
VO = ((N-1)*N)/2;
% Vector overlap

%% Preallocation
T = zeros(1,T1); Theta1 = zeros(T1-1,T1-1); Theta2 = zeros(T1-1,T1-1);
Pre1 = zeros(T1-1,T1-1); x_approx = zeros(length(times));
y_approx = zeros(length(times));
x = zeros(length(DE),length(A),length(MS),length(D));
y = zeros(length(DE),length(A),length(MS),length(D));
xp = zeros(length(DE),length(A),length(MS),length(D));
yp = zeros(length(DE),length(A),length(MS),length(D));
errx = zeros(length(DE),length(A),length(MS),length(D));
erry = zeros(length(DE),length(A),length(MS),length(D));
S1 = zeros(length(DE),length(A),length(MS),length(D));
S2 = zeros(length(DE),length(A),length(MS),length(D));
S3 = zeros(length(DE),length(A),length(MS),length(D));
STDx = zeros(length(DE),length(A),length(MS),length(D));
STDy = zeros(length(DE),length(A),length(MS),length(D));
xi = zeros(T1-1,T1-1,times); yi = zeros(T1-1,T1-1,times);
warning off

%% Loop
tic
for r1 = 1:length(DE)
    for r2 = 1:length(A)
        for r3 = 1:length(MS)
            for r4 = 1:length(D)
```

```
                err = DE(r1);
% +/- xx degrees error
                d = MS(r3);
% Current microphone separation distance
                r = D(r4);
% Current sound source to array distance
                ang = A(r2);
% Current angle
                deltMax = (T1-1)/4;
                for t = 1:times
                    for n1 = 1:T1
% Calculate primary row thetas (including error)
                        T(n1) = atan(sin(ang)/(cos(ang)+.5*((((M-1)...
                            /2)*d-d*(n1-1))/r)))+randn(1)*err*(pi/180);
                    end
                    for n2 = 1:T1-1
% Create Theta combination matrices with error
                        Theta1(n2:T1-1,n2) = T(n2);
                        Theta2(n2,1:n2) = T(n2+1);
                        Pre1(n2:T1-1,n2) = 1;
                    end
                    col1 = d/2:d/2:d/2+(T1-2)*(d/2);
                    col2 = repmat(((deltMax*d-d/2)*(-
1):d/2:(deltMax*d...
                        -d/2)*(-1)+(T1-2)*(d/2))',[1,T1-1]);
                    aM = toeplitz(col1,zeros(1,T1-1));
% 'a' Matrix
                    PreM = Pre1.*col2;
% 'Pre' Matrix
                    xi(:,:,t) = PreM+(aM.*tan(Theta1))./(tan(Theta2)-
...
                        tan(Theta1));
                    yi(:,:,t) = aM.*tan(Theta1).*tan(Theta2)./...
                        (tan(Theta2)-tan(Theta1));
                    x_approx(t) = nanmean(nanmean(xi(:,:,t)));
                    y_approx(t) = nanmean(nanmean(yi(:,:,t)));
                end
                x(r1,r2,r3,r4) = mean(x_approx);
% Approximated x location
                y(r1,r2,r3,r4) = mean(y_approx);
% Approximated y location
                xp(r1,r2,r3,r4) = r*cos(ang);
% Actual x location
                yp(r1,r2,r3,r4) = r*sin(ang);
% Actual y location
                errx(r1,r2,r3,r4) = abs(x(r1,r2,r3,r4)-
xp(r1,r2,r3,r4))...
                    /r*100;
% Error x-direction [%]
                erry(r1,r2,r3,r4) = abs(y(r1,r2,r3,r4)-
yp(r1,r2,r3,r4))...
                    /r*100;
% Error y-direction [%]
                S1(r1,r2,r3,r4) = MS(r3);
% Sensor 1 x-location
                S3(r1,r2,r3,r4) = -MS(r3);
% Sensor 3 x-location
```

```
                STDx(r1,r2,r3,r4) = mean(nanmean(std(xi,0,3)));
                STDy(r1,r2,r3,r4) = mean(nanmean(std(yi,0,3)));
                clc
                Percent_r1 = ((r1-1)/length(DE))*100;
                Percent_r2 = ((r2-1)/length(A))*100;
                Percent_r3 = ((r3-1)/length(MS))*100;
                Percent_r4 = ((r4-1)/length(D))*100;
                disp(['Percent_r1 = ' num2str(Percent_r1)])
                disp(['Percent_r2 = ' num2str(Percent_r2)])
                disp(['Percent_r3 = ' num2str(Percent_r3)])
                disp(['Percent_r4 = ' num2str(Percent_r4)])
            end
        end
    end
end

%% Plot
MS1 = 10;
MS2 = 10;
MS3 = 8;
var1 = [1,2,3,1,2,3,1,2,3];
% Hardcoded
var2 = [1,1,1,2,2,2,3,3,3];
% Hardcoded
for p = 1:length(A)^2;
% Assuming all parameters have equal length
    fig = figure('Position',[10 350 600 300]);
    figure(fig)
    hold on
    plot(x(1,1,var1(p),var2(p)),y(1,1,var1(p),var2(p)),'xb',...
        'MarkerSize',MS3);
% Plot to establish legend (if changed, must change below)
    plot(x(2,1,var1(p),var2(p)),y(2,1,var1(p),var2(p)),'db',...
        'MarkerSize',MS3);
% Plot to establish legend (if changed, must change below)
    plot(x(3,1,var1(p),var2(p)),y(3,1,var1(p),var2(p)),'sb',...
        'MarkerSize',MS3);
% Plot to establish legend (if changed, must change below)
    legend([num2str(DE(1)),'\circ Error'],[num2str(DE(2)),...
        '\circ Error'],[num2str(DE(3)),'\circ Error'],'Location',...
        'NorthWest')
% Legend
    plot(PreM(1,1)-d:d:PreM(1,1)-d+(M-1)*d,zeros(1,M),'xk',...
        'MarkerSize',MS1,'LineWidth',2)
% Sesnor position
    plot(xp(1,1,1,var2(p)),yp(1,1,1,var2(p)),'ob','MarkerSize',MS2,...
        'LineWidth',2,'MarkerFaceColor','r')
% Actual position
    plot(xp(1,2,1,var2(p)),yp(1,2,1,var2(p)),'og','MarkerSize',MS2,...
        'LineWidth',2,'MarkerFaceColor','r')
% Actual position
    plot(xp(1,3,1,var2(p)),yp(1,3,1,var2(p)),'oc','MarkerSize',MS2,...
        'LineWidth',2,'MarkerFaceColor','r')
% Actual position
    plot(x(1,1,var1(p),var2(p)),y(1,1,var1(p),var2(p)),'xb',...
```

```
        'MarkerSize',MS3,'LineWidth',1);
% Replot to put on top of actual position (if changed, must change
above)
    plot(x(2,1,var1(p),var2(p)),y(2,1,var1(p),var2(p)),'db',...
        'MarkerSize',MS3,'LineWidth',1);
% Replot to put on top of actual position (if changed, must change
above)
    plot(x(3,1,var1(p),var2(p)),y(3,1,var1(p),var2(p)),'sb',...
        'MarkerSize',MS3,'LineWidth',1);
% Replot to put on top of actual position (if changed, must change
above)
    plot(x(1,2,var1(p),var2(p)),y(1,2,var1(p),var2(p)),'xg',...
        'MarkerSize',MS3,'LineWidth',1);
% Estimated position
    plot(x(2,2,var1(p),var2(p)),y(2,2,var1(p),var2(p)),'dg',...
        'MarkerSize',MS3,'LineWidth',1);
% Estimated position
    plot(x(3,2,var1(p),var2(p)),y(3,2,var1(p),var2(p)),'sg',...
        'MarkerSize',MS3,'LineWidth',1);
% Estimated position
    plot(x(1,3,var1(p),var2(p)),y(1,3,var1(p),var2(p)),'xc',...
        'MarkerSize',MS3,'LineWidth',1);
% Estimated position
    plot(x(2,3,var1(p),var2(p)),y(2,3,var1(p),var2(p)),'dc',...
        'MarkerSize',MS3,'LineWidth',1);
% Estimated position
    plot(x(3,3,var1(p),var2(p)),y(3,3,var1(p),var2(p)),'sc',...
        'MarkerSize',MS3,'LineWidth',1);
% Estimated position
    xlabel('Distance (cm)');
    ylabel('Distance (cm)');
    errorbar(x(1,1,var1(p),var2(p)),y(1,1,var1(p),var2(p)),...
        STDy(1,1,var1(p),var2(p)),'-b')
    errorbar(x(2,1,var1(p),var2(p)),y(2,1,var1(p),var2(p)),...
        STDy(2,1,var1(p),var2(p)),'-b')
    errorbar(x(3,1,var1(p),var2(p)),y(3,1,var1(p),var2(p)),...
        STDy(3,1,var1(p),var2(p)),'-b')
    errorbar(x(1,2,var1(p),var2(p)),y(1,2,var1(p),var2(p)),...
        STDy(1,2,var1(p),var2(p)),'-g')
    errorbar(x(2,2,var1(p),var2(p)),y(2,2,var1(p),var2(p)),...
        STDy(2,2,var1(p),var2(p)),'-g')
    errorbar(x(3,2,var1(p),var2(p)),y(3,2,var1(p),var2(p)),...
        STDy(3,2,var1(p),var2(p)),'-g')
    errorbar(x(1,3,var1(p),var2(p)),y(1,3,var1(p),var2(p)),...
        STDy(1,3,var1(p),var2(p)),'-c')
    errorbar(x(2,3,var1(p),var2(p)),y(2,3,var1(p),var2(p)),...
        STDy(2,3,var1(p),var2(p)),'-c')
    errorbar(x(3,3,var1(p),var2(p)),y(3,3,var1(p),var2(p)),...
        STDy(3,3,var1(p),var2(p)),'-c')
    herrorbar(x(1,1,var1(p),var2(p)),y(1,1,var1(p),var2(p)),...
        STDy(1,1,var1(p),var2(p)),'-b')
    herrorbar(x(2,1,var1(p),var2(p)),y(2,1,var1(p),var2(p)),...
        STDy(2,1,var1(p),var2(p)),'-b')
    herrorbar(x(3,1,var1(p),var2(p)),y(3,1,var1(p),var2(p)),...
        STDy(3,1,var1(p),var2(p)),'-b')
    herrorbar(x(1,2,var1(p),var2(p)),y(1,2,var1(p),var2(p)),...
        STDy(1,2,var1(p),var2(p)),'-g')
```

```
    herrorbar(x(2,2,var1(p),var2(p)),y(2,2,var1(p),var2(p)),...
        STDy(2,2,var1(p),var2(p)),'-g')
    herrorbar(x(3,2,var1(p),var2(p)),y(3,2,var1(p),var2(p)),...
        STDy(3,2,var1(p),var2(p)),'-g')
    herrorbar(x(1,3,var1(p),var2(p)),y(1,3,var1(p),var2(p)),...
        STDy(1,3,var1(p),var2(p)),'-c')
    herrorbar(x(2,3,var1(p),var2(p)),y(2,3,var1(p),var2(p)),...
        STDy(2,3,var1(p),var2(p)),'-c')
    herrorbar(x(3,3,var1(p),var2(p)),y(3,3,var1(p),var2(p)),...
        STDy(3,3,var1(p),var2(p)),'-c')
    hold off
    title(['Microphone Separation (',num2str(MS(var1(p))),...
        ' cm), Distance (',num2str(D(var2(p))),' cm), ',num2str(M),...
        '-Mic Array']);
    saveas(fig,strcat(['Fig.',num2str(p),' MS = ',num2str(var1(p)),...
        '; D = ',num2str(var2(p))],'.bmp'),'bmp')
    saveas(fig,strcat(['Fig.',num2str(p),' MS = ',num2str(var1(p)),...
        '; D = ',num2str(var2(p))],'.fig'),'fig')
end
close all

warning on
toc
```

where herrorbar is a subfunction developed by Jos van der Geest and available on MATLAB Central File Exchange

```
function hh = herrorbar(x, y, l, u, symbol)
%HERRORBAR Horizontal Error bar plot.
%   HERRORBAR(X,Y,L,R) plots the graph of vector X vs. vector Y with
%   horizontal error bars specified by the vectors L and R. L and R
contain the
%   left and right error ranges for each point in X. Each error bar
%   is L(i) + R(i) long and is drawn a distance of L(i) to the right
and R(i)
%   to the right the points in (X,Y). The vectors X,Y,L and R must all
be
%   the same length. If X,Y,L and R are matrices then each column
%   produces a separate line.
%
%   HERRORBAR(X,Y,E) or HERRORBAR(Y,E) plots X with error bars [X-E
X+E].
%   HERRORBAR(...,'LineSpec') uses the color and linestyle specified by
%   the string 'LineSpec'. See PLOT for possibilities.
%
%   H = HERRORBAR(...) returns a vector of line handles.
%
%   Example:
%      x = 1:10;
%      y = sin(x);
%      e = std(y)*ones(size(x));
%      herrorbar(x,y,e)
%   draws symmetric horizontal error bars of unit standard deviation.
%
%   This code is based on ERRORBAR provided in MATLAB.
%
```

```
%   See also ERRORBAR

%   Jos van der Geest
%   email: jos@jasen.nl
%
%   File history:
%   August 2006 (Jos): I have taken back ownership. I like to thank
Greg Aloe from
%   The MathWorks who originally introduced this piece of code to the
%   Matlab File Exchange.
%   September 2003 (Greg Aloe): This code was originally provided by
Jos
%   from the newsgroup comp.soft-sys.matlab:
%   http://newsreader.mathworks.com/WebX?50@118.fdnxaJz9btF^1@.eea3ff9
%   After unsuccessfully attempting to contact the orignal author, I
%   decided to take ownership so that others could benefit from finding
%   it on the MATLAB Central File Exchange.

if min(size(x))==1,
    npt = length(x);
    x = x(:);
    y = y(:);
    if nargin > 2,
        if ~isstr(l),
            l = l(:);
        end
        if nargin > 3
            if ~isstr(u)
                u = u(:);
            end
        end
    end
else
    [npt,n] = size(x);
end

if nargin == 3
    if ~isstr(l)
        u = l;
        symbol = '-';
    else
        symbol = l;
        l = y;
        u = y;
        y = x;
        [m,n] = size(y);
        x(:) = (1:npt)'*ones(1,n);;
    end
end

if nargin == 4
    if isstr(u),
        symbol = u;
        u = l;
    else
        symbol = '-';
```

```
    end
end

if nargin == 2
    l = y;
    u = y;
    y = x;
    [m,n] = size(y);
    x(:) = (1:npt)'*ones(1,n);;
    symbol = '-';
end

u = abs(u);
l = abs(l);

if isstr(x) | isstr(y) | isstr(u) | isstr(l)
    error('Arguments must be numeric.')
end

if ~isequal(size(x),size(y)) | ~isequal(size(x),size(l)) |
~isequal(size(x),size(u)),
    error('The sizes of X, Y, L and U must be the same.');
end

tee = (max(y(:))-min(y(:)))/100; % make tee .02 x-distance for error
bars
% changed from errorbar.m
xl = x - l;
xr = x + u;
ytop = y + tee;
ybot = y - tee;
n = size(y,2);
% end change

% Plot graph and bars
hold_state = ishold;
cax = newplot;
next = lower(get(cax,'NextPlot'));

% build up nan-separated vector for bars
% changed from errorbar.m
xb = zeros(npt*9,n);
xb(1:9:end,:) = xl;
xb(2:9:end,:) = xl;
xb(3:9:end,:) = NaN;
xb(4:9:end,:) = xl;
xb(5:9:end,:) = xr;
xb(6:9:end,:) = NaN;
xb(7:9:end,:) = xr;
xb(8:9:end,:) = xr;
xb(9:9:end,:) = NaN;

yb = zeros(npt*9,n);
yb(1:9:end,:) = ytop;
yb(2:9:end,:) = ybot;
```

```
yb(3:9:end,:) = NaN;
yb(4:9:end,:) = y;
yb(5:9:end,:) = y;
yb(6:9:end,:) = NaN;
yb(7:9:end,:) = ytop;
yb(8:9:end,:) = ybot;
yb(9:9:end,:) = NaN;
% end change


[ls,col,mark,msg] = colstyle(symbol); if ~isempty(msg), error(msg); end
symbol = [ls mark col]; % Use marker only on data part
esymbol = ['-' col]; % Make sure bars are solid

h = plot(xb,yb,esymbol); hold on
h = [h;plot(x,y,symbol)];

if ~hold_state, hold off; end

if nargout>0, hh = h; end
```

Appendix D

The purpose of Appendix D is to provide a proof of concept for an optical microphone developed and fabricated in precisely the same way as the microphone detailed in the thesis. The difference is a reduced size. The capillary tube, instead of having an outer diameter of 360 μm and inner diameter of 150 μm will have dimensions of 166 μm and 100 μm, respectively. The smaller capillary tube requires the use of a custom 80 μm fiber. Figure 0-1 provides a size comparison between the two sensors.

Figure 0-1. Size comparison of 166 μm outer diameter sensor (left), and 360 μmFigure 0-2. Size comparison of 166 μm outer diameter sensor (left), and 360 μmFigure 0-3. Size comparison of 166 μm

The performance of the smaller sensor is less refined than that of its bigger sibling, as shown in indicated by the frequency sweep presented in Figure 0-2.

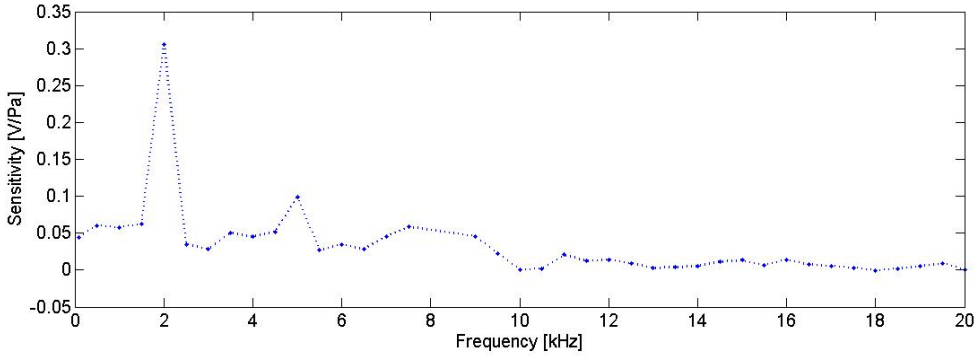

Figure 0-5. Frequency response of 100 μm diameter optical microphone.

Bibliography

1. N. Tandon and A. Choudhury, "A review of vibration and acoustic measurement methods for the detection of defects in rolling element bearings," Tribology International **32**, 469-480 (1999).

2. K. Kageyama, H. Murayama, I. Ohsawa, M. Kanai, K. Nagata, Y. Machijima, and F. Matsumura, "Acoustic emission monitoring of a reinforced concrete structure by applying new fiber-optic sensors," Smart Materials and Structures **14**, 552-559 (2005).

3. P. Mcdonald, D. Geraghty, I. Humphreys, and S. Farrell, "of Transport Noise with Wireless Sensor Networks," Transportation Research Record 133-139 (2008).

4. B. Kaushik, D. Nance, and K. K. Ahuja, "A Review of the Role of Acoustic Sensors," in *11th AIAA/CEAS Aeroacoustics Conference (26th AIAA Aeroacoustics Conference)* (2005).

5. J. Fraden, "Handbook of Modern Sensors," in *Sensors (Peterborough, NH)* (Springer New York, 2010), pp. 431-443.

6. M. Yu, "Fiber-optic sensor system for acoustic measurements," University of Maryland, College Park (2002).

7. C. F. Hess, "Optical microphone for the detection of hidden helicopters," AIAA Journal **30**, 2626-2631 (1992).

8. L. H. Chen, C. C. Chan, W. Yuan, S. K. Goh, and J. Sun, "High performance chitosan diaphragm-based fiber-optic acoustic sensor," Sensors & Actuators: A. Physical **163**, 42-47 (2010).

9. T. Yoshino, K. Kurosawa, K. Itoh, and T. Ose, "Fiber-Optic Fabry-Perot Interferometer and Its Sensor Applications," IEEE Journal of Quantum Electronics **18**, 1624-1633 (1982).

10. M. Han, X. Wang, J. Xu, K. L. Cooper, and W. Anbo, "Diaphragm-based extrinsic Fabry-Perot interferometric optical fiber sensor for acoustic wave detection under high background pressure," Optical Engineering **44**, (2005).

11. X. Wang, B. Li, Z. Xiao, S. H. Lee, H. Roman, O. L. Russo, K. K. Chin, and K. R. Farmer, "An ultra-sensitive optical MEMS sensor for partial discharge detection," Journal of Micromechanics and Microengineering **15**, 521-527 (2005).

12. M. Yu and B. Balachandran, "Acoustic Measurements Using a Fiber Optic Sensor System," Journal of Intelligent Material Systems and Structures **14**, 409-414 (2003).

13. J. Xu, X. Wang, K. L. Cooper, and A. Wang, "Miniature all-silica fiber optic pressure and acoustic sensors," Optics Letters **30**, 3269-3271 (2005).

14. B. Yu, D. W. Kim, J. Deng, H. Xiao, and A. Wang, "Fiber Fabry-Perot sensors for detection of partial discharges in power transformers," Applied Optics **42**, 3241-3250 (2003).

15. N. Fuerstenau, H. Horack, and W. Schmidt, "Extrinsic Fabry-Perot interferometer fiber-optic microphone," IEEE Transactions on Instrumentation and Measurement **47**, 138-142 (1998).

16. K. K. Chin, Y. Sun, G. Feng, G. E. Georgiou, K. Guo, E. Niver, H. Roman, and K. Noe, "Fabry-Perot diaphragm fiber-optic sensor," Applied Optics **46**, 7614-7619 (2007).

17. S. C. Ko, C.-H. Jun, W. I. Jang, and C.-A. Choi, "Micromachined air-gap structure MEMS acoustic sensor using reproducible high-speed lateral etching and CMP process," Journal of Micromechanics and Microengineering **16**, 2071-2076 (2006).

18. G. He and F. W. Cuomo, "Displacement Response, Detection Limit, and Dynamic Range of Fiber-Optic Lever Sensors," Journal of Lightwave Technology **9**, 1618-1625 (1991).

19. G. He, "The analysis of noises in a fiber optic microphone," **92**, 2521-2526 (2011).

20. A. Hu and A. J. Zuckerwar, "Theoretical and experimental study of a fiber optic microphone --," **91**, 3049-3056 (1992).

21. G. He and M. T. Wlodarczyk, "Catheter-type disposable fiber optic pressure transducer," in *Proceedings of the 9th Optical Fiber Sensors Conference* (1993), pp. 463-466.

22. A. J. Zuckerwar, F. W. Cuomo, T. D. Nguyen, S. A. Rizzi, and S. A. Clevenson, "High-temperature fiber-optic lever microphone," Journal of the Acoustical Society of America **97**, 3605-3616 (1995).

23. J. A. Bucaro and N. Lagakos, "Lightweight fiber optic microphones and accelerometers," Review of Scientific Instruments **72**, 2816-2821 (2001).

24. A. Sun, Z. Wu, C. Wan, and C. Yang, "All-fiber optic acoustic sensor based on multimode-single mode-multimode structure," Optik - International Journal for Light and Electron Optics (2011).

25. T. Iida, K. Nakamura, and S. Ueha, "A Microphone Array using Fiber Bragg Gratings," in *15th Optical Fiber Sensors Conference Technical Digest* (2002), Vol. 1, pp. 239-242.

26. L. Mohanty, L. M. Koh, and S. C. Tjin, "Fiber Bragg grating microphone system," Applied Physics Letters **89**, (2006).

27. J. N. Fields, "Coupled waveguide acoustooptic hydrophone," Applied Optics **18**, 3533-3534 (1979).

28. E. F. Carome and K. P. Koo, "Multimode coupled waveguide acoustic sensors," Optics Letters **5**, 359-361 (1980).

29. R. Chen, G. F. Fernando, T. Butler, and R. A. Badcock, "A novel ultrasound fibre optic sensor based on a fused-tapered optical fibre coupler," Measurement Science and Technology **15**, 1490-1495 (2004).

30. R. Chen, T. Bradshaw, R. Badcock, P. Cole, P. Jarman, D. Pedder, and G. F. Fernando, "Linear location of acoustic emission using a pair of novel fibre optic sensors," Journal of Physics: Conference Series **15**, 232-236 (2005).

31. R. Chen, T. Bradshaw, J. Burns, P. Cole, P. Jarman, D. Pedder, R. Theobald, and G. F. Fernando, "Linear location of acoustic emission using a pair of novel fibre optic sensors," Measurement Science and Technology **17**, 2313-2318 (2006).

32. W. B. Spillman and D. H. McMahon, "Frustrated-total-internal-reflection multimode fiber-optic hydrophone," Applied Optics **19**, 113-117 (1980).

33. R. L. Phillips, "Proposed fiber-optic acoustical probe," Optics Letters **5**, 318-320 (1980).

34. W. B. Spillman and R. L. Gravel, "Moving fiber-optic hydrophone," Optics Letters **5**, 30-31 (1980).

35. G. A. Rines, "Fiber-optic accelerometer with hydrophone applications," Applied Optics **20**, 3453-3459 (1981).

36. W. B. Spillman, "Multimode fiber-optic hydrophone based on a schlieren technique," Applied Optics **20**, 465-470 (1981).

37. W. B. Spillman and D. H. McMahon, "Schlieren multimode fiber-optic hydrophone," Applied Physics Letters **37**, 145-147 (1980).

38. B. W. Tietjen, "The optical grating hydrophone," The Journal of the Acoustical Society of America **69**, 993-997 (1981).

39. J. N. Fields, C. K. Asawa, O. G. Ramer, and M. K. Barnoski, "Fiber optic pressure sensor," Journal of the Acoustical Society of America **67**, 816-818 (1980).

40. J. N. Fields and J. H. Cole, "Fiber microbend acoustic sensor," Applied Optics **19**, 3265-3267 (1980).

41. N. Lagakos, T. Litovitz, P. Macedo, R. Mohr, and R. Meister, "Multimode optical fiber displacement sensor," Applied Optics **20**, 167-168 (1981).

42. N. Lagakos, W. J. Trott, T. R. Hickman, J. H. Cole, and J. A. Bucaro, "Microbend fiber-optic sensor as extended hydrophone," IEEE Journal of Quantum Electronics **18**, 1633-1638 (1982).

43. E. Cibula and D. Donlagić, "Miniature fiber-optic pressure sensor with a polymer diaphragm," Applied Optics **44**, 2736-2744 (2005).

44. G. Wild and S. Hinckley, "Acousto-Ultrasonic Optical Fiber Sensors: Overview and State-of-the-Art," IEEE Sensors Journal **8**, 1184-1193 (2008).

45. G. He and F. W. Cuomo, "The analysis of noises in a fiber optic microphone," Journal of the Acoustical Society of America **92**, 2521-2526 (1992).

46. A. Hu, F. W. Cuomo, and A. J. Zuckerwar, "Theoretical and experimental study of a fiber optic microphone," Journal of the Acoustical Society of America **91**, 3049-3056 (1992).

47. J. A. Bucaro, N. Lagakos, and B. H. Houston, "Miniature, high performance, low-cost fiber optic microphone," Journal of the Acoustical Society of America **118**, 1406-1413 (2005).

48. S. L. Gay and J. Benesty, *Acoustic Signal Processing for Telecommunication* (Kluwer Academic, 2000).

49. T. F. Brooks and W. M. Humphreys, "Effect of directional array size on the measurement of airframe noise components," in *Fifth AIAA/CEAS Aeroacoustics Conference* (1999).

50. J. Benesty, J. Chen, and Y. Huang, *Microphone Array Signal Processing* (Springer Verlag, 2008).

51. T. D. Jick, "Mixing Qualitative and Quantitative Methods: Triangulation in Action," Administrative Science Quarterly **24**, 602-611 (1979).

52. R. N. Miles, D. Robert, and R. R. Hoy, "Mechanically coupled ears for directional hearing in the parasitoid fly Ormia ochracea," The Journal of the Acoustical Society of America **98**, 3059-3070 (1995).

53. D. Robert, R. N. Miles, and R. R. Hoy, "Directional hearing by mechanical coupling in the parasitoid fly Ormia ochracea," Journal of Comparative Physiology. A, Sensory, Neural, and Behavioral Physiology **179**, 29-44 (1996).

54. a P. Lisiewski, H. J. Liu, M. Yu, L. Currano, and D. Gee, "Fly-ear inspired micro-sensor for sound source localization in two dimensions.," The Journal of the Acoustical Society of America **129**, EL166-71 (2011).

55. H. J. Liu, M. Yu, and X. M. Zhang, "Biomimetic optical directional microphone with structurally coupled diaphragms," Applied Physics Letters **93**, 243902 - 243902-3 (2008).

56. R. N. Miles, Q. Su, W. Cui, M. Shetye, F. L. Degertekin, B. Bicen, C. Garcia, S. Jones, and N. Hall, "A low-noise differential microphone inspired by the ears of the parasitoid fly Ormia ochracea," The Journal of the Acoustical Society of America **125**, 2013-2026 (2009).

57. M. Touse, J. Sinibaldi, K. Simsek, J. Catterlin, S. Harrison, and G. Karunasiri, "Fabrication of a microelectromechanical directional sound sensor with electronic readout using comb fingers," Applied Physics Letters **96**, 173701 (2010).

58. M. Yu, X. Long, and B. Balachandran, "Sensor diaphragm under initial tension: Nonlinear responses and design implications," Journal of Sound and Vibration **312**, 39-54 (2008).

59. Y. Zhu and A. Wang, "Miniature Fiber-Optic Pressure Sensor," IEEE Photonics Technology Letters **17**, 447-449 (2005).

60. K. Totsu, Y. Haga, and M. Esashi, "Ultra-miniature fiber-optic pressure sensor using white light interferometry," Journal of Micromechanics and Microengineering **15**, 71-75 (2005).

61. K. Grattan and B. Meggitt, *Optical Fiber Sensor Technology: Fundamentals* (Kluwer Academic Publishers, 2000).

62. M. Yu and B. Balachandran, "Sensor Diaphragm Under Initial Tension□: Linear Analysis Linear Model of Plate with Tension Free Oscil ations of Undamped System," Experimental Mechanics 123-129 (n.d.).

63. A. Lisiewski, "Fly-Ear Inspired Miniature Sensor System for Two-Dimensional Sound Source Localization," University of Maryland, College Park (2011).

64. S. Ando, T. Kurihara, K. Watanabe, Y. Yamanishi, and T. Ooasa, "Novel theoretical design and fabrication test of biomimicry directional microphone," IEEE Transducers 1932-1935 (2009).

65. L. Currano, H. Liu, D. Gee, B. Yang, and M. Yu, "Microscale implementation of a bio-inspired acoustic localization device," in *SPIE 2009 Symposium on Defense, Security, and Sensing* (2009).

66. M. Yu, "Fiber-Optic sensor systems for acoustic measurements," University of Maryland, College Park (2002).

67. Brüel & Kjær, "Type 4191 Product Data," http://www.bksv.com/doc/bp2212.pdf?document=/doc/bp2212.pdf&r=http://www.google.com/url?sa=t&rct=j&q=&esrc=s&source=web&cd=3&ved=0CGMQFjAC&url=http://www.bksv.com/doc/bp2212.pdf&ei=2n-sT5PTL_Kd6AGig_iwBA&usg=AFQjCNH6jzLTbsI0KVnGQBydO7YR9pMldg&sig2=-v3G9oN0Z-AnZ3nVY_JC6w.

68. Akustica, "AKU340 Analog MEMS Microphone," http://www.akustica.com/Files/Admin/PDFs/DS26-0.91 AKU340 Preliminary Datasheet.pdf.

69. C.-H. Huang, C.-H. Lee, T.-M. Hsieh, L.-C. Tsao, S. Wu, J.-C. Liou, M.-Y. Wang, L.-C. Chen, M.-C. Yip, and W. Fang, "Implementation of the CMOS MEMS condenser microphone with corrugated metal diaphragm and silicon back-plate.," Sensors (Basel, Switzerland) **11**, 6257-6269 (2011).